BAMS Supplement

Aerosol–Ice Formation Closure

A Southern Great Plains Field Campaign

D. A. Knopf, K. R. Barry, T. A. Brubaker, L. G. Jahl, K. A. Jankowski, J. Li, Y. Lu, L. W. Monroe, K. A. Moore, F. A. Rivera-Adorno, K. A. Sauceda, Y. Shi, J. M. Tomlin, H. S. K. Vepuri, P. Wang, N. N. Lata, E. J. T. Levin, J. M. Creamean, T. C. J. Hill, S. China, P. A. Alpert, R. C. Moffet, N. Hiranuma, R. C. Sullivan, A. M. Fridlind, M. West, N. Riemer, A. Laskin, P. J. DeMott, and X. Liu

https://doi.org/10.1175/BAMS-D-20-0151.2
Corresponding author: D. A. Knopf, daniel.knopf@stonybrook.edu
This is a supplement to https://doi.org/10.1175/BAMS-D-20-0151.1

AFFILIATIONS: **Knopf, Li, Lu, and Wang**—Stony Brook University, State University of New York, Stony Brook, New York; **Barry, Moore, Levin, Creamean, Hill, and DeMott**—Colorado State University, Fort Collins, Colorado; **Brubaker, Jahl, Monroe, and Sullivan**—Carnegie Mellon University, Pittsburgh, Pennsylvania; **Jankowski, Rivera-Adorno, Tomlin, and Laskin**—Purdue University, West Lafayette, Indiana; **Sauceda, Vepuri, and Hiranuma**—West Texas A&M University, Canyon, Texas; **Shi and Liu**—Texas A&M University, College Station, Texas; **Lata and China**—Environmental Molecular Sciences Laboratory, Pacific Northwest National Laboratory, Richland, Washington; **Alpert**—Laboratory of Environmental Chemistry, Paul Scherrer Institute, Villigen, Switzerland; **Moffet**—Sonoma Technology, Inc., Petaluma, California; **Fridlind**—NASA Goddard Institute for Space Studies, New York, New York; **West and Riemer**—University of Illinois at Urbana–Champaign, Urbana, Illinois

Online instrumentation. **SMPS**. The scanning mobility particle sizer (SMPS) was composed of a DMA model 3082 equipped with 0.0457-cm impactor and CPC model 3775 (TSI Inc.). Aerosol was sampled directly from the high-volume stack via 3/8-in. outer diameter (OD) tubing at 0.3 SLPM aerosol flow and 3.0 SLPM (standard liter per minute) sheath flow. For the last segment of the aerosol sampling line, 1/4-in. OD tubing was used. The aerosol flow passed through a diffusion dryer filled with silica gel that was replaced daily to dry the flow to a relative humidity below 10%. The aerosol size distribution was measured in scanning mode every 4 min from 14.6 to 750 nm in mobility diameter. The full measurement range of the instrument was not used due to sampling noise as outlined in the "Merging size distributions from SMPS and APS instruments" section.

APS. The aerodynamic particle sizer (APS) (model 3321, TSI Inc.) sampled directly from the high-volume stack via 3/8-in. OD tubing at 5.0 SLPM (1.0 SLPM aerosol flow and 4.0 SLPM sheath flow). Particle concentrations were measured every 4 min from 0.49 to 20.5 μm in aerodynamic diameter. In contrast to the SMPS instrument, the aerosol flow through the APS was not dried. The procedure to merge SMPS and APS data are described in the "Particle loss estimates" section below. The full measurement range of the instrument was not used due to sampling noise as outlined in the "Merging size distributions from SMPS and APS instruments" section.

SP-AMS. The Soot-Particle Aerosol Mass Spectrometer (SP-AMS) sampled directly from the high-volume stack via 1/4-in. OD tubing at 0.1 SLPM. The aerosol flow entering SP-AMS was not dried. It has an optional IR laser for vaporization of soot-containing particles equipped on a high-resolution time-of-flight (HR-TOF) AMS, but the laser module was nonfunctional upon arriving at the campaign (Corbin et al. 2014; Dallmann et al. 2014; Onasch et al. 2012). The AMS therefore only measured submicron nonrefractory organic and inorganic components using thermal desorption by the conventional 600°C heater, followed by 70 eV electron ionization and the time-of-flight mass analyzer operated in V mode. Size-resolved particle composition is determined by particle time of flight from the aerosol chopper when using pToF mode. Data were averaged every 4 min and analyzed using Igor software packages SQUIRREL (version 1.62A) and PIKA (version 1.22A) with ionization efficiencies and sizing parameters based on calibrations using atomized, dried, and size-selected ammonium nitrate particles.

LAAPTOF. The Laser Ablation Aerosol Particle Time-of-Flight Mass Spectrometer (LAAPTOF) sampled from the aerosol concentrator via 1/4-in. OD tubing at 0.1 SLPM with an extra bypass flow that pulled 1.0 SLPM close to the instrument inlet to reduce aerosol residence time in the sampling line. The aerosol flow entering LAAPTOF was not dried. The LAAPTOF combines laser velocimetry for aerodynamic particle sizing with UV laser desorption/ionization for bipolar time-of-flight mass spectrometry to measure individual particle composition (Gemayel et al. 2016; Murphy 2007; Pratt and Prather 2012; Shen et al. 2018; Sullivan and Prather 2005). Particle velocities were calibrated versus size using polystyrene latex spheres of known diameters. The LAAPTOF can detect essentially any particle component of interest in these experiments via 193-nm UV laser ablation by the excimer laser. This is especially important for biological, soot, and mineral dust particles that are not ordinarily detected by the AMS. Raw data conversion to stick spectra was conducted on the LAAPTOF data analysis software from Aeromegt GmbH (version 0.1.7). Ward-based exclusive hierarchical clustering was conducted after preprocessing the stick spectra by taking the square root, in MATLAB 2019a using built-in and custom functions and code (Rebotier and Prather 2007). The Fuzzy-C nonexclusive clustering algorithm built into the Aeromegt GmbH software was not used to avoid double counting of particles that may interfere with modeling inputs (Reitz et al. 2016).

WIBS. The Wideband Integrated Bioaerosol Sensor 4A (WIBS-4A) or WIBS (Droplet Measurement Technologies) for short, was used to collect information on fluorescent and biological aerosols. Most biological particles contain compounds that fluoresce at wavelengths detected by this technology, and most nonbiological particles fluoresce weakly or at different wavelengths. Therefore, the WIBS may be used to distinguish fluorescent particles that are predominantly biological from particles that are predominantly nonbiological (Pöhlker et al. 2012). The WIBS gives fluorescence information on single particles in three channels: A (fluorescence at 310–400 nm, excited at 280 nm), B (fluorescence at 420–650 nm, excited at 280 nm), and C (fluorescence at 420–650 nm, excited at 370 nm). Seven possible combinations of fluorescent emission response may be determined, as discussed by Perring et al. (2015). Background fluorescence values in each channel in the absence of particles were measured daily. Only particles with fluorescence values greater than 2.5 standard deviations above the daily mean background value are reported here (Twohy et al. 2016). Total particle concentrations were also determined based on scattered light from a 635-nm diode laser, which occurs in advance of the fluorescence measurements. Particles below 0.8 μm were removed from the dataset, as particles smaller than this are at or below the limit of detection for the WIBS PMTs with their current gain setting (Perring et al. 2015). Following Twohy et al. (2016), two estimates for the concentration of fluorescent biological aerosol particles (FBAPs) were archived: particles that fluoresce in both channels A and C (AC_ABC; more conservative), and particles that fluoresce in either channel A or channel C (non-B; less conservative). The air sample to the WIBS came from a y-splitter that connected to the entering CFDC copper sample line from the stack. A small section of flexible conductive tubing transferred particles to the WIBS. No particle drying was directly applied but drying likely occurred in bringing air into the laboratory and into the optical cavity.

PINE-c. The Portable Ice Nucleation Experiment chamber (PINE-c) instrument used in this study is a commercially available instrument version developed by Karlsruhe Institute of Technology in technical collaboration with University of Leeds and Bilfinger Noell (Würzburg, Germany) mainly for the following two purposes: 1) to promote long-term and remote ambient INP concentration monitoring in a semiautonomous manner via network and 2) to study atmospheric ice formation through an adiabatic expansion process in a ~10-L aluminum vessel, where an artificial cloud is formed at temperatures relevant to atmospheric heterogeneous ice nucleation (Möhler et al. 2021). The design and fundamental concept of PINE-c are based on the Aerosol Interactions and Dynamics in the Atmosphere (AIDA) chamber (Möhler et al. 2003). (Möhler et al. 2003). PINE-c allows autonomous and continuous operation and has the capability of quantifying INPs in different ice nucleation modes (deposition nucleation and immersion freezing), a detection sensitivity per experiment of 0.25–50,000 INP L^{-1} STP with 6–10-min time resolution and small particle loss through the system (~20% for <2-μm diameter particles). The chamber is equipped with six temperature sensors across the vessel as well as an automated temperature controlling function (e.g., ramping between –5° and –35°C set-point temperatures every 90 min repeatedly). With a reasonable temporal resolution (a turn-over time of about 6–10 min for subsequent expansions), this instrument allows for a single expansion to compute INP number concentrations over a range of approximately 4°–5°C without notable artifact from background ice formation, as it operates with frost-free walls. During the field campaign daily background ice formation tests were conducted. It was found that those were negligible having no effect on measured INP number concentrations. Note that parallel twin Perma Pure Nafion dryers were always run at approximately 100 hPa to strip off the incoming moisture in the sampled air due to the pressure gradient between ambient air and dryers. The application of dryers was necessary to prevent frost formation in the PINE-c. Varying the temperature and water saturation condition determines what

nucleation mode occurs within the chamber. Detection of ice crystals occurs while particles are drawn through an optical particle counter (OPC) (fidas-pine, Palas GmbH, Karlsruhe, Germany), which records the particle count and particle diameter in the ~0.7–220-μm optical size range (with 256 channels resolution). PINE-c has been successfully validated against the AIDA chamber implying that no further correction of INP number concentrations need to be applied (Möhler et al. 2021).

Here, PINE-c data represent cumulative INP number concentrations (per liter of air at STP) during each expansion, which takes 79.0 ± 2.1 s (average ± standard deviation). During the adiabatic expansion, the air cools in a nonlinear manner to the desired lowest freezing temperature. During this study, the total temperature decrease in individual expansions was 4.7° ± 2.1°C. The current uncertainty involved in the PINE-c measurement in terms of temperature is ±1°C (Möhler et al. 2021). The PINE-c temperature reported in this study is based on the middle gas temperature, which often resulted in the coldest temperature within the given uncertainty, for the ambient and experimental conditions during Aerosol–Ice Formation Closure Pilot Study (AEROICESTUDY). The INP number concentration uncertainty is based on the systematic error of the OPC (±20%). During our field campaign, the PINE-c instrument sampled directly from the high-volume stack via 3/8-in. diameter copper tubing (total length of 98 in.) at 2 SLPM.

To estimate the nucleation time to predict INP number concentrations following classical nucleation theory [activity-based immersion freezing model (ABIFM)], we chose accumulated INP number concentration during the coldest 2°C (reflecting the temperature uncertainty) of the expansion. The time it takes the expansion to yield this lowest temperature interval is used as the corresponding nucleation time. At the end of the expansion, the temperature change with time is smallest. As the initial temperature at which an expansion start changes, so does the time needed for expansion to cool by 2°C. This yields the stated range in nucleation times applied in the closure calculations that are dependent on the chosen coldest freezing temperatures. For each measured INP number concentration the associated nucleation time is considered in the respective closure calculation.

CFDC. The CSU Continuous Flow Diffusion Chamber (CFDC) operating principles are described previously (Rogers 1988; Rogers et al. 2001) and is detailed in the form used in this study by DeMott et al. (2018). This cylindrical ice thermal diffusion chamber has been used in numerous airborne and ground-based campaigns over the course of 25 years and has served as the basis for testing and developing ice nucleation parameterizations in the past. New developments have made it possible to operate the instrument in a nearly autonomous and continuous manner (Bi et al. 2019). Ice crystals forming on INPs over a ~5-s period at calculated T and RH conditions in the upper chamber region enter the lower "evaporation" section of the chamber where ice temperatures are adjusted to evaporate any liquid droplets while ice crystals continue to grow to detection at larger sizes. To assist ice identification, aerosols entering the CFDC are limited by a two-stage impactor to below 2.5-μm aerodynamic diameter (50% "cut" size), such that all particles measured in size bins above ~4 μm in the OPC at the base of the CFDC are considered as ice crystals. The CFDC was operated well into the water-supersaturated regime (105%–107% RH) in order to favor immersion freezing nucleation (DeMott et al. 2018). Interval time periods during which the aerosol sample is filtered were used to determine background frost influences at ice particle sizes in the OPC. Definition of statistically significant INP concentrations and confidence intervals (90% two-tailed) used particle arrival rates and sample volumes (at 1.5 LPM sample flow rate) during ambient and filter periods following Moore (2020). Consequently, although the instrument measures at 1-Hz resolution, statistically meaningful integral sampling periods typically range from 1 to a few minutes in length, as apparent in archive files for this study.

Temperature uncertainty is ±0.5°C at the reported CFDC lamina processing temperature. RH uncertainty depends inversely on temperature, and has been estimated as ±1.6%, 2%, and 2.4% at –20°, –25°, and –30°C, respectively (Hiranuma et al. 2015). The CFDC sampled directly from the high-volume stack via mixed 1/4-in. OD copper and conductive tubing lines and was located in close proximity to the main aerosol entry port and other instrument systems in the GIF. Particles were always dried with diffusion dryers (typically to less than 5% RH at room temperature) prior to passing the 2.5-μm impactor couplet upstream of entry into the CFDC.

An aerosol concentrator (Model 4240, MSP Corporation) was used at times upstream of the CFDC and the LAAPTOF instrument to enhance aerosol number concentrations to improve measurement statistics and collection of aerosols and INP composition information. The concentration factor achieved depends on the aerosols and INP size distributions (Tobo et al. 2013) and is determined by the ratio of the concentration using the concentrator versus concentrations from the ambient inlet. This factor was determined as a daily average in this study when correcting CFDC data for archival during periods of concentrator use. The concentrator was placed on the observation deck outside of the GIF at the same height as the high-volume stack intake. The outlet flow was passed at the flow rate drawn by the instruments through a 1/4-in. OD copper line ran with minimal bend into the GIF, where valves were used to send particles to the CFDC or LAAPTOF. A typical procedure was to operate the CFDC for 10 min on the ambient inlet, 5 min on filter, and 10 min on the concentrator. Longer periods on the concentrator alone were used for collecting grids for Scanning Transmission Electron Microscopy (STEM) analyses (Suski et al. 2018).

Grids of activated INPs were collected using a custom single-jet impactor with a 50% cut size of ~4 μm, to align with the ice crystal detection size and to provide a bias against capture of any unfrozen particles at sizes that would pass the upstream CFDC inlet impactor. STEM analyses are in process at the time of this writing.

Offline instrumentation. **MOUDI**. Multi Orifice Uniform Deposition Impaction (MOUDI) (model MOUDI-II Impactor 122R) sampled via a 1-in. OD tubing at 30 SLPM close to the high-volume stack. The MOUDI is an impactor with 13 rotating stages with cutoff diameters (0.010, 0.018, 0.032, 0.056, 0.10, 0.18, 0.32, 0.56, 1.0, 1.8, 3.2, 5.6, and 10 μm). It allows for collection of size-resolved ambient aerosol onto substrates (Si_3N_4 waver chips and TEM grids) suitable for microspectroscopic analyses such as computer-controlled (CC) scanning electron microscopy (SEM) with energy dispersive X-ray (EDX) spectroscopy, scanning transmission X-ray microscopy (STXM) coupled with near-edge X-ray absorption fine structure spectroscopy (NEXAFS), and ice nucleation experiments (Knopf et al. 2014; Wang et al. 2012). This yields morphological and compositional characterization of the aerosol population on a scale of tenths of nanometer (Knopf et al. 2018, 2014; Laskin et al. 2016; Moffet et al. 2016; O'Brien et al. 2015; Wang et al. 2012).

CCSEM/EDX and SEM/EDX analysis was performed at the Environmental Molecular Sciences Laboratory (EMSL)/Pacific Northwest National Laboratory (PNNL). CCSEM/EDX provides the analysis of a large number of particles for elemental composition and morphology (Hopkins et al. 2007, 2008; Laskin et al. 2006, 2019, 2016). Particles with an equivalent circle diameter larger than 0.2 μm are characterized. The particle types present in the ambient aerosol population are derived using the *k*-means cluster analysis as shown in Fig. ES7 (Cheng 1995; Fukunaga and Hostetler 1975; Knopf et al. 2014; Moffet et al. 2013; Selim and Ismail 1984).

STXM/NEXAFS analysis was performed at the Advanced Light Source at Lawrence Berkeley National Laboratory at beamlines 5.3.2.2 and 11.0.2. STXM/NEXAFS allows examination of the chemical composition and mixing states of individual particles by measuring

the transmission of soft X-ray beams generated from the synchrotron light source with a spatial resolution of about 30 nm (Ghorai and Tivanski 2010; Ghorai et al. 2011; Kilcoyne et al. 2003; Moffet et al. 2010a,b). Application of the carbon K-edge energy range allows the identification of organic carbon (OC), elemental carbon (EC; i.e., soot), potassium (K), and other overall contribution of inorganic components (IN) within individual particles. Derived particle composition maps are based on absorption energies 285.4 and 288.6 eV representing C–C double bonds (EC, soot) and carboxylic groups (OC). Pre- and postedge (278 and 320 eV) are used to derive total inorganic and organic fractions (Knopf et al. 2014; Moffet et al. 2016; O'Brien et al. 2015). Derivation of the organic volume fraction follows the method outlined by Fraund et al. (2019).

MOUDI-DFT. Multi Orifice Uniform Deposition Impaction Droplet Freezing Technique (MOUDI-DFT) employs size-resolved aerosol collected on Si_3N_4 waver chips by MOUDI to probe for immersion freezing INPs. The experiment follows Mason et al. (2015). In short, our controlled vapor cooling stage microscope system (Knopf et al. 2011, 2014) is used to induce water uptake and droplet formation in sizes of about 40 μm. Once the droplets formed, the ice nucleation cell is sealed, and the droplet sample is cooled with 10°C min^{-1} until all droplets are frozen. Freezing and corresponding freezing temperatures are detected by optical microscopy via digital imaging analysis (Alpert et al. 2011; Rigg et al. 2013). We used particles collected on stage 4 (cutoff: 1.8 μm) and assumed uniform deposition across 1 mm of substrate corroborated by applied microscopy (e.g., Fig. ES9). Typical temperature uncertainty is ±0.3°C, thus, INP number concentrations are reported in minimum 0.6°C intervals. Uncertainty in INP number concentrations are derived from the upper and lower fiducial limits of nucleation events (Alpert and Knopf 2016; Knopf et al. 2020; Koop et al. 1997). Two hundred and fifty droplets forming ice were observed and used in the analysis. Background ice nucleation events were determined by monitoring freezing of micrometer-sized water droplets, expressed as frozen fraction (Fig. ES16).

DRUM-CP. Size-resolved aerosol was collected via impaction using a Davis Rotating-drum Unit for Monitoring coupled with a Cold Plate (DRUM-CP) for size-resolved bulk immersion freezing. The DRUM-CP combines collection of aerosol particles at four size ranges (i.e., from 0.13 to >12 μm in diameter with size cuts at 5.0, 2.6, and 0.75 μm) during sampling at ~30 L min^{-1} onto substrates within a DRUMAir (Cahill et al. 1987) impactor with immersion freezing measurements of resuspended particles in microliter-sized droplets on a cold plate device (Creamean et al. 2019, 2018a,b,c). Air was drawn in though the DRUM on its own inlet that was approximately the same height as the main laminar sampling stack that was mounted to the GIF observation platform. Aerosols were impacted onto clean perfluoroalkoxy substrate strips coated with petrolatum, a material that contains very few artifacts that interfere with the INP analysis (Creamean et al. 2018b). The substrate strips were adhered to discs in each size chamber that rotated slowly over time, developing a "smear" of aerosol loading over 5 mm. After 24 h, the discs rotated an additional 2 mm quickly leaving a blank spot in between each daily sample. Sample substrate strips were stored at –20°C until offline processing. The time period of the DRUM daily sample sets (i.e., four sizes per period) analyzed for their INP concentration spectra were selected as appropriate for other instrument sampling periods, or for the full 24-h periods, by cutting the substrate strips under sterile conditions (i.e., using single-use scalpels in a laminar benchtop hood). Particles were released from substrate segments using 2 mL of deionized water in a vortex mixer for at least 20 min followed by placement of one hundred 2.5-μL drop aliquots on a CP that is cooled at 3°–10°C min^{-1} until all drops freeze or until the CP limit of –27°C is achieved. Drop freezing is detected and recorded through monitoring software to provide the freezing temperature and cooling

rate for each drop. Experiments are repeated for three 100-drop series for each sample. Serial dilutions in deionized water were used to count INPs active at the lowest temperatures. Analyses of freezing spectra follow Vali (1971). Background INP number concentrations are given in Fig. ES16.

IS. Immersion freezing INP concentrations were also measured from total aerosol (i.e., all sizes) using the Colorado State University (CSU) Ice Spectrometer (IS). The IS instrument is a measurement device with well-established experimental protocols (DeMott et al. 2018). A filter sampler comprised of a vacuum pump pulling at 16–18 L min^{-1} was mounted approximately 6 m above ground level on the sampling deck outside of the GIF, at a level coincident with the main sampling inlet. Single-use filter units open to the atmosphere fitted with presterilized polycarbonate filters (0.2 μm) fitted within sterile Nalgene filter units were covered by a precipitation shield. Filters were typically drawn for either a full day period (0900–1700 CDT) or broken up into morning (0900–1200 CDT) and afternoon (1300–1700 CDT) periods. Additionally, four overnight filters were taken (1800–0800 CDT). Filters were stored at –20°C until offline processing. Following total particle resuspension into a total volume of 8 mL, frozen wells in 32 aliquots of 50 μL were counted at 1-min intervals as temperature was lowered at 0.33°C min^{-1} to a –28°C limit. Serial dilutions in deionized water were used to count INPs active at lower temperatures. Two semiautomated (software cooling control and a CCD camera) IS systems were used. Portions of aerosol suspensions were treated to isolate total biological, organic, and inorganic INPs. To assess the fractional contribution of heat labile (i.e., biological) entities, such as proteinaceous INPs, a 2 mL aliquot of suspension was retested in the IS after heating to 95°C for 20 min (McCluskey et al. 2018). To remove all organic INPs, 1 mL of 30% H_2O_2 was added to a 2-mL aliquot of suspension and the mixture heated to 95°C for 20 min while illuminated with UVB fluorescent bulbs to generate hydroxyl radicals (residual H_2O_2 removed using catalase) (Suski et al. 2018), and the INPs were again assessed in the IS. Remaining INPs are likely to be mineral. Analyses of freezing spectra follow Vali (1971). Procedural controls of the sampling substrates will provide quantitative information on the signal to noise ratio to correct for background artifacts, and 95% binomial-sampling confidence intervals are determined following Agresti and Coull (1998). Background INP number concentrations are given in Fig. ES16.

Microfluidic ice nucleation technique. Aerosol particles were collected using a filter sampler comprised of a vacuum pump pulling at 16–18 SLPM that was mounted approximately 6 m above ground level on the sampling deck outside of the GIF, at a level coincident with the main sampling stack intake; 0.2-μm pore size Nuclepore filters were housed in 47-mm inline stainless steel filter holders (Pall) and were stored following collection in a freezer until analysis. Aerosol filter samples were typically collected for either a full day period (0900–1700 CDT) or broken up into morning (0900–1200 CDT) and afternoon (1300–1700 CDT) periods, and four overnight filters were also taken (1800–0800 CDT). Filter collection periods typically coincided with the filter collection periods of the CSU IS.

Just prior to analysis, the collected particles were extracted off of each filter by vortexing the filter in a polypropylene Falcon tube with 3 mL of HPLC-grade water that was prefiltered (Anotop 25 Plus 0.02-μm pore size, Whatman 6809-4102) (Brubaker et al. 2020; Jahn et al. 2020). This suspension was then filled into a custom microfluidic chip. The Microfluidic Ice Nucleation Technique (MINT) uses a "store-and-create" approach to generate uniformly sized water droplets completely suspended in squalene oil that contain particles of interest (Brubaker et al. 2020). Up to 720 6-nL droplets containing a suspended particle sample of interest can be produced and sent through a cooling cycle typically at 1°C min^{-1} to determine the droplet freezing temperature spectrum. The small droplet volume and lack of contact with

any substrate provides a low background freezing temperature for purified water controls that permits immersion freezing analysis from 0° to −33°C. Analysis of the measured droplet freezing temperature spectrum to determine $n_s(T)$ and INP L^{-1} follows the procedures outlined in Brubaker et al. (2020) and Polen et al. (2018), based on those of Vali (1971, 2019). Background ice nucleation events are expressed as frozen fraction in Fig. ES16.

The CAM6

The Community Atmospheric Model, version 6 (CAM6), the atmosphere component of the National Center for Atmospheric Research (NCAR) Community Earth System Model, version 2 (CESM2) (Danabasoglu et al. 2020), is used in this study. Aerosols in CAM6 are predicted by the four-mode version of Modal Aerosol Module (MAM4) (Liu et al. 2016). Six aerosol species are treated by MAM4, including mineral dust, sea salt, sulfate, primary organic aerosol, secondary organic aerosol, and black carbon. Mineral dust particles are carried in Aitken, accumulation, and coarse modes, which account for dust with diameter up to ~10 μm. Mineral dust emissions are calculated online depending on model wind friction velocity and land surface parameters (e.g., soil moisture and land use type) (Zender et al. 2003). The emitted dust size distribution follows the brittle fragmentation theory (Kok 2011). Soil dust emissions from agricultural activities are not accounted for by the model. Emissions for sulfur dioxide, primary organic aerosol, and black carbon are prescribed for the year 2019 under the Shared Socioeconomic Pathways (SSP) 2–4.5 scenario.

The model was driven by the Modern-Era Retrospective Analysis for Research and Applications, version 2 (MERRA-2), meteorology (Gelaro et al. 2017) and run at 0.9° × 1.25° horizontal resolution and 56 vertical layers (from surface to around 2 hPa) with prescribed climatological sea surface temperature and sea ice. The simulation was performed from 1 August to 31 October 2019, with the first two months used for model spinup. Meteorological parameters and aerosol properties were outputted at each model time step (30 min). Model mineral dust aerosol number concentrations (>0.5 μm) and total dust surface area in accumulation and coarse modes are fed into two ice nucleation parameterizations, DeMott et al. (2015) and Niemand et al. (2012), respectively, to diagnose the INP number concentrations offline. We do not apply an upper limit to the size of the simulated mineral dust aerosols when calculating the INP concentrations.

Particle loss estimates

In this pilot study we used the particle loss calculator by von der Weiden et al. (2009) to estimate particles losses in the sampling lines. The particle size distributions (PSDs) measured by the SMPS and APS serve as the input for the closure calculations. The theoretically derived particle losses in the sampling lines to the SMPS and APS are then ratioed against the theoretically derived particle losses in the sampling lines for PINE-c and CFDC instruments. Subsequently, the PSDs entering the online INP instruments were adjusted for the differences in particle losses and for the instrument particle cutoff sizes. It was beyond the scope of this pilot study to conduct an in-depth sampling inlet characterization for all the different employed online and offline instruments. However, we performed some particle loss analyses that indicated that we very likely did not experience significant particle losses.

We have compared our measured PSDs by SMPS and APS with the onsite ARM SGP Aerosol Observation System (AOS) measured PSDs. Figure ES11 displays example PSD measurements by AEROICESTUDY and SGP AOS employed SMPS and APS instruments. These data demonstrate that for particle sizes up to 5 μm (maximum size applied in our closure calculations) we have good agreement between the PSDs in our sampling lines inside the GIF instrument trailer and the ones determined by SGP AOS. This suggests that particle losses are minor as indicated by the particle loss calculations.

We conducted an additional test, where we examined particle losses through the PINE-c sampling inlet through a copper sampling inlet (3/8-in. OD; 98-in. length) connected to the vertical sampling stack. We deployed an optical particle sizer (OPS; TSI 3330) and a condensation particle counter (CPC; TSI 3007) on the deck of SGP-GIF besides the stack inlet and inside at the exit of the sampling inlet to determine the PSD of ambient particles that pass through the total sampling line (stack and sampling inlet). We measured ambient aerosol concentrations on the deck using OPC and CPC before and after measuring the particles at the sampling inlet. This sequence was employed to make sure that we probe similar air masses. Our size distribution data (Fig. ES12) suggest that PSDs measured in ambient air and through stack and sampling line are very consistent. We observed upper 5-μm volume equivalent diameter (D_{ve}) particles at the sampling inlet of PINE-c while a slight suppression of >8-μm D_{ve} particles is observed. The CPC measurements indicate a particle transmission of about 79%. The loss of about 20% of particles can be attributed to diffusional loss of particles smaller than 0.3 μm.

These particle loss evaluations support that negligible particle losses have occurred during aerosol particle sampling. For a full campaign study, we recommend employing well-characterized sampling stacks and sampling inlets.

Merging size distributions from SMPS and APS instruments

To produce a merged size distribution that covers the entire range of SMPS and APS instruments, the aerodynamic diameter measured by the APS needs to be converted to mobility diameter measured by the SMPS, using the following conversion (Khlystov et al. 2004):

$$D_p = D_a \sqrt{\chi \frac{\rho_0}{\rho_p}} = \frac{D_a}{x}.$$

Here D_p and D_a are the mobility and aerodynamic diameters, respectively, ρ_p is the density of the aerosol, ρ_p is the reference density (1,000 kg m^{-3}) and χ is the shape factor. The factor x is called the size-correction factor.

Procedures for such a size distribution merging are documented in Khlystov et al. (2004) and Beddows et al. (2010). However, these methods could not be directly applied for our purposes because the size distributions measured during our campaign did not exhibit overlap between the SMPS and the APS size ranges. This was the case for the instruments operated both at the ARM SGP site and by AEROICESTUDY. Additionally, a comparison of the APS data at the sampling stack with APS data from the SGP site showed that the APS instrument at the stack systematically undercounted particles in the size range below 0.8 μm, which made the gap between SMPS and APS size ranges even larger. We therefore used data from the SMPS and APS at the SGP site to derive the size-correction factor. This involved the following steps:

Since the SGP APS data are sampled every second, it was averaged within 5 min intervals so that it matched the sample frequency of the SGP SMPS data. A lognormal function was fitted to the accumulation mode of the distribution measured by the SGP SMPS using observations in the size range 0.1 μm < D_p < 0.4 μm. The data from the first five SGP APS size bins (aerodynamic diameter smaller than 0.7 μm) were discarded. We denote the diameter and observed number concentration of the sixth APS size bin by $D_{a,\mathrm{APS},6}$ and $n_{\mathrm{APS},6}$, respectively. The corresponding mobility diameter $D_{p,\mathrm{APS},6}$ was determined so that the point ($D_{p,\mathrm{APS},6}$, $n_{\mathrm{APS},6}$) lay on the fitted lognormal curve. The size-correction factor x was then calculated as $x = D_{a,\mathrm{APS},6}/D_{p,\mathrm{APS},6}$. For the 15 October case, the average size-correction factor was 1.4, which corresponds to an average effective density, ρ_p/χ, of 1,900 kg m^{-3}.

This size-correction factor was then applied to the APS data from the sampling stack. This involved: The sampling times of the stack SMPS, APS data and size-correction factor were

unified by interpolation of all data onto the 4-min stack SMPS time stamps. The aerodynamic stack APS diameters were converted to mobility diameters using the size-correction factor. An issue of consideration is that the aerosol flow in the SMPS instrument was dried while the flow in the APS instrument was not dried. The application of the size correction factor accounts for this. Everything else being equal, at higher relative humidity, the gap between the (dry) SMPS size distribution and the APS size distribution tends to be larger, which will be taken into account by a larger correction factor. The stack APS and SMPS data were interpolated onto a unified logarithmic grid of mobility diameters. To eliminate the noise present near the edges of the sampling ranges in the stack SMPS and APS, we discarded SMPS data for mobility diameters larger than 0.2 μm and APS data for aerodynamic diameters smaller than 0.8 μm (thus discarding the first 7 APS bins). A Gaussian process regressor was applied to interpolate data in this transition range using all data points outside the transition range with number concentration at least 10^{-3} cm^{-3} and a regularizing additional diagonal variance of $\alpha = 10^{-16}$ cm^{-6}. Number concentrations and surface area concentrations for the closure were calculated from these postprocessed size distributions.

Immersion freezing parameterizations

The underlying physical assumptions that make up various immersion freezing parameterizations are a matter of discussion in the community. The two most popular approaches are the singular hypothesis, also termed deterministic description, and classical nucleation theory (CNT) (e.g., Knopf et al. 2018; Vali et al. 2015). The singular hypothesis description assumes that certain particle features, also called ice-active sites, initiate ice nucleation governed only by temperature (Vali 1971). This can then be scaled with aerosol particle number concentration or with INP surface area, the latter is also known as the ice-active site density (INAS) (Connolly et al. 2009). Ice formation can be described using CNT that accounts, besides the temperature dependency, for the stochastic nature of nucleation and its time dependence (Pruppacher and Klett 1997). It also scales with the INP surface area.

In this closure study, we apply two immersion freezing parameterizations that are founded in the assumptions of the singular hypothesis and one parameterization that follows CNT. This allows us to examine different types of immersion freezing parameterizations to predict ice crystal formation under given conditions.

We apply the INP parameterization by DeMott et al. (2010) that is based on several field campaign measurements of INP number concentrations, mostly by aircraft. For this reason, it encompasses various particle types and is not INP composition specific. This parameterization is based on the singular hypothesis description and allows prediction of INP number concentrations for given aerosol number concentration for particles larger than 0.5 μm. The INP data forming the basis for this parameterization were obtained using an upper size limit ~1.6 μm. Hence application of this parameterization for larger particle sizes may introduce a bias in INP number concentrations.

The INP parameterization by DeMott et al. (2015) is for application to natural mineral dust particles. It was derived from laboratory experiments using Saharan and Asian desert dusts and field measurements in two scenarios dominated by the same. Its functional relationship between INP number concentration and number of mineral dust particles is similar to the parameterization of DeMott et al. (2010). It is based on the singular hypothesis description and only the number of mineral dust particles larger than 0.5 μm is needed for prediction of INP number concentrations.

We apply the INAS description that is based on the singular hypothesis approach (Connolly et al. 2009) and previous laboratory studies (China et al. 2017; Knopf and Alpert 2013; Niemand et al. 2012; Schill et al. 2020). It is specific to the INP composition and scales with the INP surface area. The concept is that for lower temperatures, more ice-active sites

become available that can initiate ice formation. Furthermore, as the INP surface area increases, more ice-active sites are available, thereby increasing the number of ice nucleation events. Application of this parameterization requires detailed information of aerosol composition and size.

We apply the water ABIFM (Knopf and Alpert 2013) and previous studies (Alpert and Knopf 2016; Knopf and Alpert 2013). ABIFM represents an INP parameterization following CNT parameterized with respect to ambient humidity and temperature, the latter both are expressed by the water activity criterion (Koop et al. 2000). In this study we assume water saturation (i.e., the water activity equals 1) and the INP is engulfed in supercooled water. It is specific to the INP composition and scales with the INP surface area and freezing time. The freezing time can be considered as the time the INP is exposed to a given supersaturation with respect to ice. Application of this parameterization requires detailed information of aerosol composition and size and instrument specific freezing times.

ABIFM soot parameterization

An ABIFM soot parameterization applicable for the closure calculations was not available. Here, we use the INAS soot parameterization by Schill et al. (2020) to obtain $J_{het}(T)$ estimates which in turn allows to derive a ABIFM parameterization. A detailed analysis of the soot immersion freezing experiments by Schill et al. (2020) to derive $J_{het}(T)$ necessitating the employed soot particle size distribution for each n_s value, similar as done in Alpert and Knopf (2016), is beyond the scope of this study. Considering that the uncertainty in the soot INAS parameterization is about plus or minus one order of magnitude, we scale reported $n_s(T)$ values by the CFDC residence times to obtain an estimate of $J_{het}(T)$. Subsequently we fit an ABIFM parameterization to those values (Fig. ES13), resulting in $m = 18.0679$ and $c = -2.0847$ with $\log_{10}(J_{het}) = c + m \times \Delta a_w$, where Δa_w represents the water activity criterion (Knopf and Alpert 2013). The term Δa_w combines relative humidity and freezing temperature in one parameter, linked via the ice melting point (Koop et al. 2000).

Uncertainty propagation for derivation on ice-nucleating particle number concentrations

We considered uncertainties in number concentration measurements and in the parameterization coefficients ("parametric uncertainties"). A summary of these uncertainties is given in Table ES2. We estimated an uncertainty in the particle number concentration (N_{tot}) of 10% across all sizes. Each type of immersion freezing parameterization has its own uncertainty since it is based on field or laboratory data. Thus, the uncertainty in reported INP number concentrations (N_{INP}) is the result of uncertainties in aerosol number concentration and immersion freezing parameterizations. Parametric uncertainties in INAS and ABIFM for aerosol mixtures (dust + org + soot) were computed as root mean squares of the parametric uncertainties (in n_s and J_{het}, respectively) for each INP type. Some parametric uncertainties depend on temperature. For temperature-dependent uncertainties, Table ES2 reports uncertainty ranges and mean values reflecting the temperature ranges probed in the closure case study. Note that number concentration uncertainties were smaller than parametric uncertainties by at least one order of magnitude. For INAS and ABIFM we calculated the INP number concentration for each size bin i as

$$N_{INP,i} = N_{tot,i}\,(1 - e^{-S_i n_s(T)}), \tag{1}$$

and

$$N_{INP,i} = N_{tot,i}\,(1 - e^{-S_i J_{het}(T) t}), \tag{2}$$

where $N_{INP,i}$ is INP number concentration in size bin i, $N_{tot,i}$ is total number concentration of specific INP type in size bin i, s_i is surface area of specific INP type in given size bin i, $n_s(T)$ is

INP type specific INAS density, $J_{het}(T)$ is INP type specific heterogeneous ice nucleation rate coefficient, and t is instrument specific freezing time. Summation over all INP instrument specific size bins yields total N_{INP}.

Table ES2 describes the contribution of uncertainties in N_{tot} and in parameters that yield N_{INP} uncertainties. The manner of propagation can be understood as follows. "Direct application" indicates that this uncertainty affects N_{INP} directly; e.g., looking at Eqs. (1) and (2), 10% uncertainty in N_{tot} will result in 10% uncertainty in N_{INP}. "Propagate through" indicates that the effect of given parametric uncertainty impacts N_{INP} via its functional dependencies, e.g., uncertainties in $n_s(T)$ and $J_{het}(T)$ affect N_{INP} not directly [see Eqs. (1) and (2)].

Parametric and number concentration uncertainties were combined multiplicatively for all parameterizations. Note that number concentration uncertainties were smaller than parametric uncertainties by at least one order of magnitude.

Uncertainties in the particle type fractions (dust versus org versus soot) for mixtures were not included. The particle-type proportions as determined by CCSEM/EDX are likely better than 1% (Thompson 1987) in the size range measured. This is because of the large particle sample probed. However, the mapping of the CCSEM/EDX identified particle types onto applied INP types of dust, org, and soot likely results in additional uncertainties that cannot be easily assessed. Also, the particle type fractions outside the CCSEM/EDX measurement size range were extrapolated and thus introduced additional uncertainty. The effective measurement size range for CCSEM/EDX is from approximately 300 nm to 3 μm. Below 350 nm, we assumed a particle population composition equal to the average composition between 350 and 500 nm. This was 0.3% dust, 13.0% soot, 86.7% organics for the morning period, and 6.8% dust, 12.8% soot, 80.4% organics for the afternoon as shown in Fig. ES14. Above 3 μm, we assumed the same composition as the largest measured size bin (100% organics for the morning period, and 100% dust for the afternoon period). Furthermore, as we have outlined, we are likely missing INP types introducing additional uncertainty. As such, particle type uncertainty can be significant.

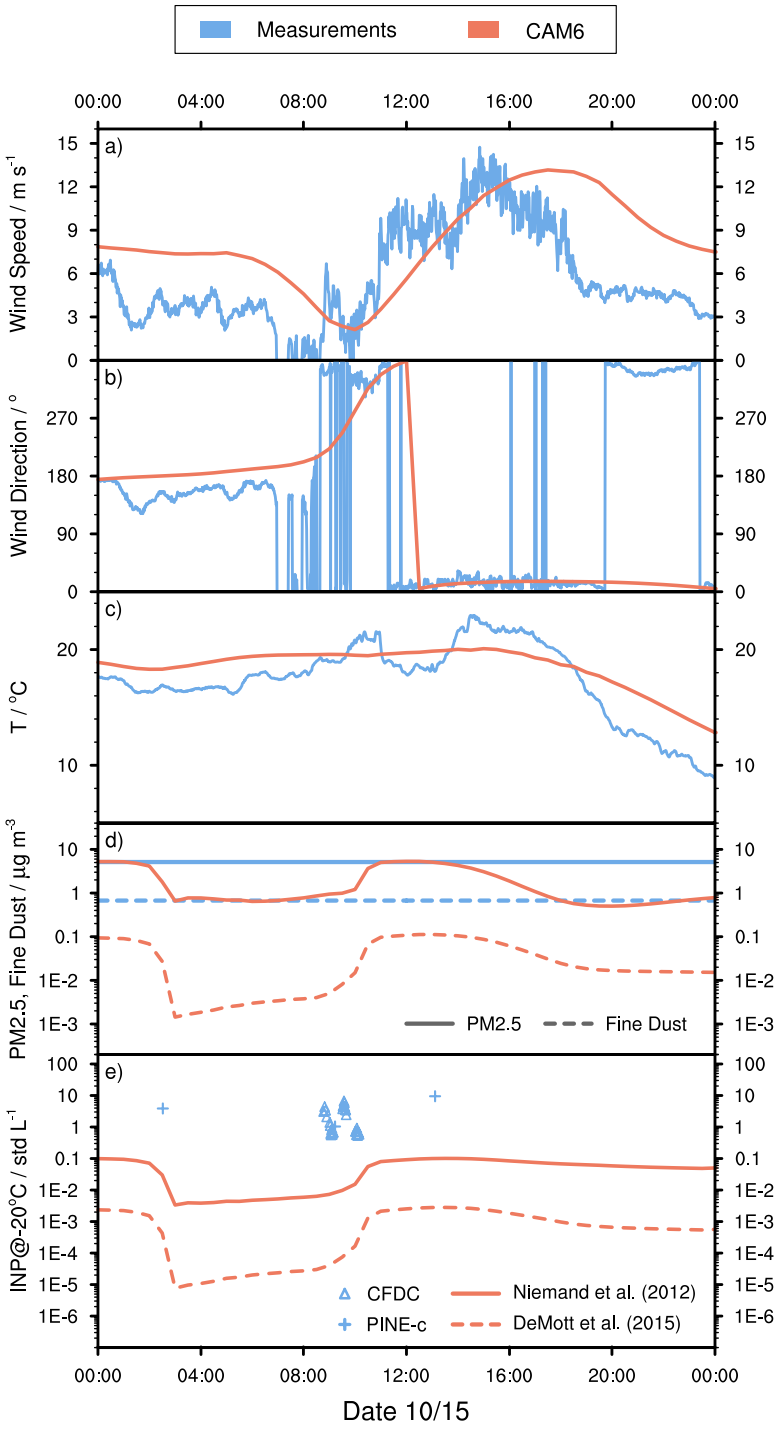

Fig. ES1. Time series of Community Atmospheric Model, version 6 (CAM6), for closure case on 15 Oct simulated (orange) and measured (blue) (a) wind speed, (b) wind direction, (c) temperature, (d) particulate matter with a diameter smaller than 2.5 μm ($PM_{2.5}$, thick lines) and dust load (thin lines), and (e) ice-nucleating particles (INPs) at –20°C during the entire field campaign. Meteorology data in (a)–(c) were obtained from DOE ARM SGP E13 station. Blue lines in (d) are the median value of Interagency Monitoring of Protected Visual Environments (IMPROVE) observation in October from 2002 to 2009 at Cherokee Nation, Oklahoma (CHER1). The thick orange line in (e) represents the parameterization by Niemand et al. (2012), and the thin orange line represents the parameterization by DeMott et al. (2015). Blue triangles and pluses are INP measurements by Continuous Flow Diffusion Chamber (CFDC) and Portable Ice Nucleation Experiment (PINE-c), respectively.

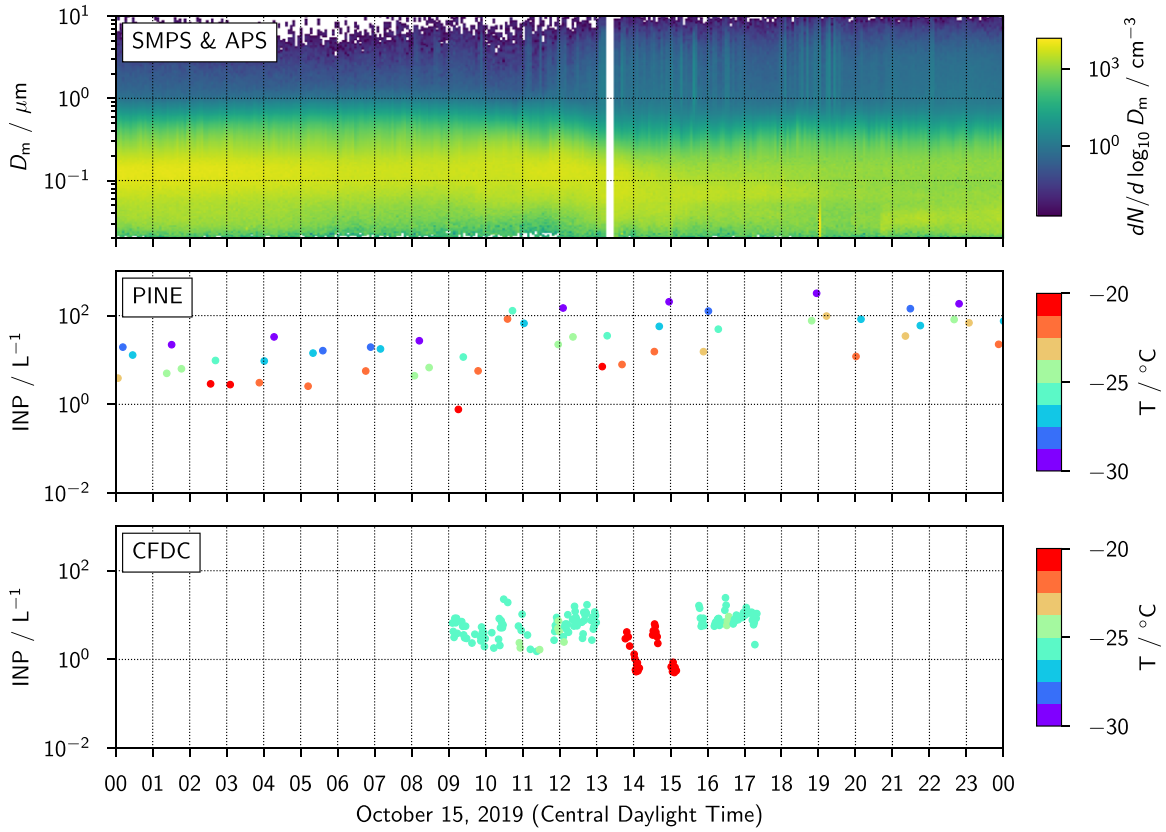

Fig. ES2. Online measurements for the closure case study on 15 Oct. (top) Particle size distributions from combined measurements by scanning mobility particle sizer (SMPS) spectrometer and aerodynamic particle sizer (APS) spectrometer and ice-nucleating particle (INP) number concentrations with associated freezing temperatures measured by (middle) PINE-c and (bottom) CFDC.

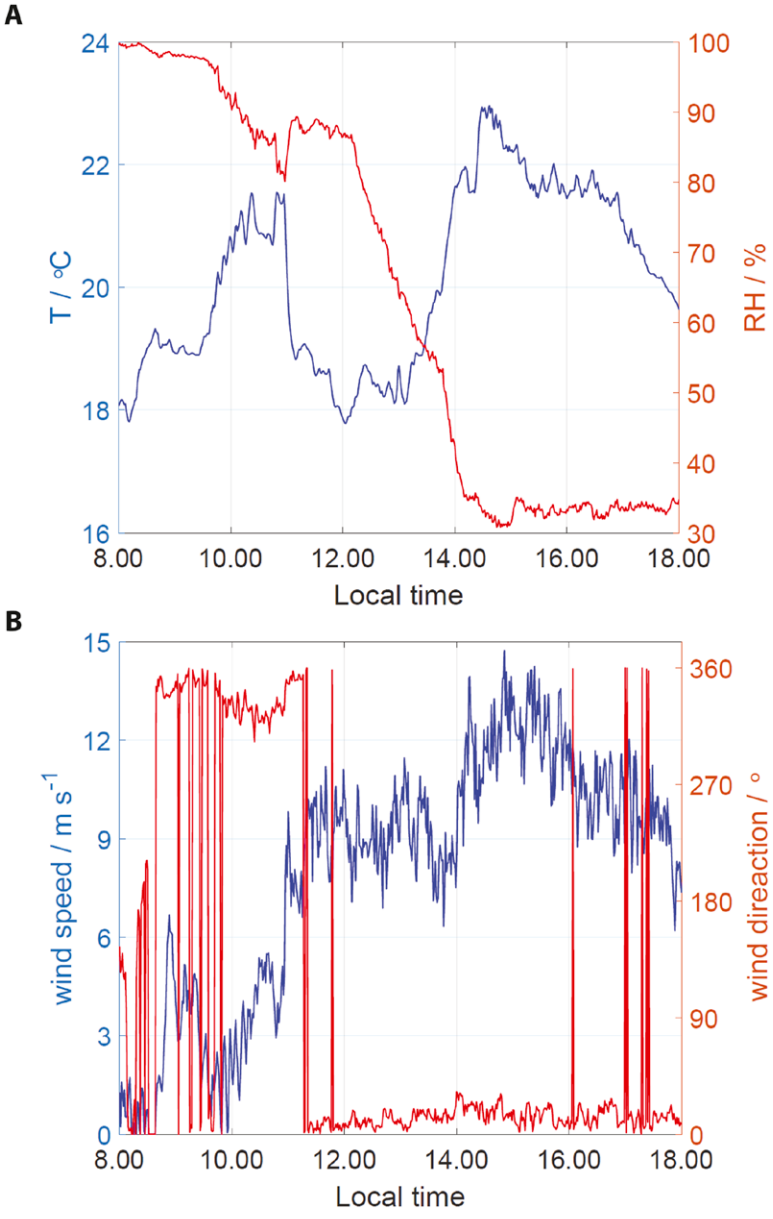

Fig. ES3. Meteorological conditions at AEROICESTUDY campaign location (U.S. DOE ARM SGP site) for frontal passage case study on 15 Oct (Kyrouac and Holdridge 2019). (a) Temperature and humidity. (b) Wind speed and direction.

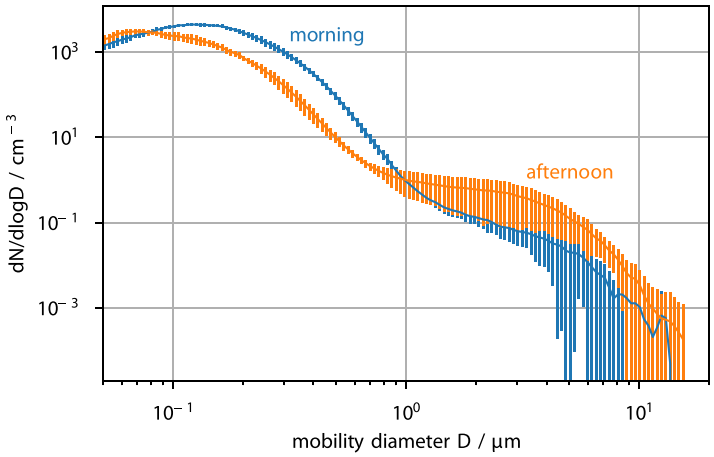

Fig. ES4. Average particle size distribution for morning hours (blue, 0800–1030 LT) and afternoon hours (orange, 1400–1800 LT) on 15 Oct, for the frontal passage case study. The error bars indicate one standard deviation around the average value.

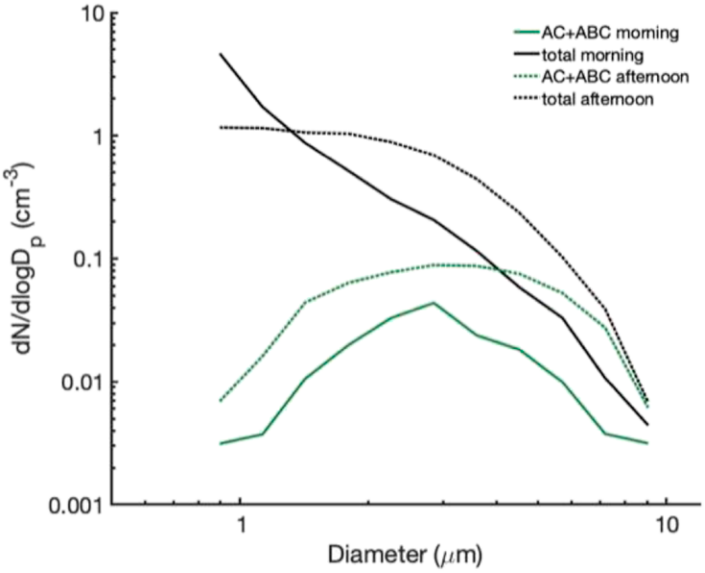

Fig. ES5. Total particle size distribution and fluorescent biological particle size distributions at sizes > 0.8 μm as measured by the WIBS instrument in morning and afternoon periods for the closure case study on 15 Oct. Classification of fluorescent biological aerosol particles (FBAPs) in this case uses the more conservative measure for particles that fluoresce in both A and C channels (see supplemental information text). Total particle concentrations are perfectly consistent with those measured by the APS in Fig. ES2. FBAP increases in the supermicron regimen in the afternoon align with increases in heat-labile INPs measured by the IS at temperatures > –20°C in the same afternoon period (Fig. ES11). The source of FBAP and INPs as being from soil or plant emissions cannot be discerned.

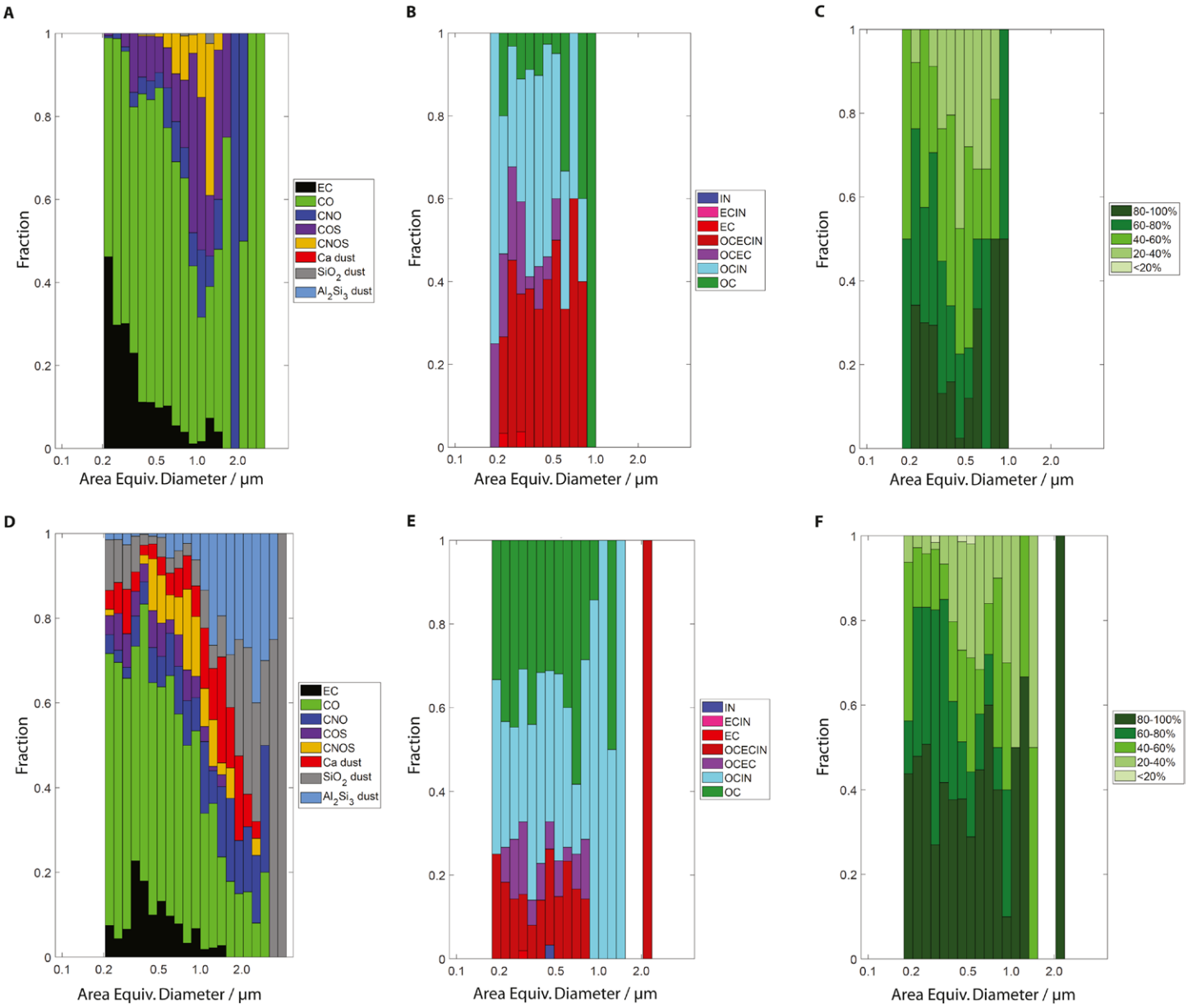

Fig. ES6. (a),(d) Size-resolved single-particle microspectroscopic analyses by computer-controlled scanning electron microscopy with energy dispersive X-ray (CCSEM/EDX) analysis providing fractional elemental particle composition where EC: elemental carbon; CO: carbon, oxygen; CNO: carbon, nitrogen, oxygen; COS: carbon, oxygen, sulfate; CNOS: carbon, nitrogen, oxygen, sulfate. Scanning transmission X-ray microscopy with near-edge X-ray absorption fine structure spectroscopy (STXM/NEXAFS) providing (b),(e) fractional particle mixing state where IN: inorganic; EC: elemental carbon; OC: organic carbon and (c),(f) organic volume fraction per particle. Ambient particle samples collected during the (top) morning and (bottom) afternoon for the closure case study on 15 Oct.

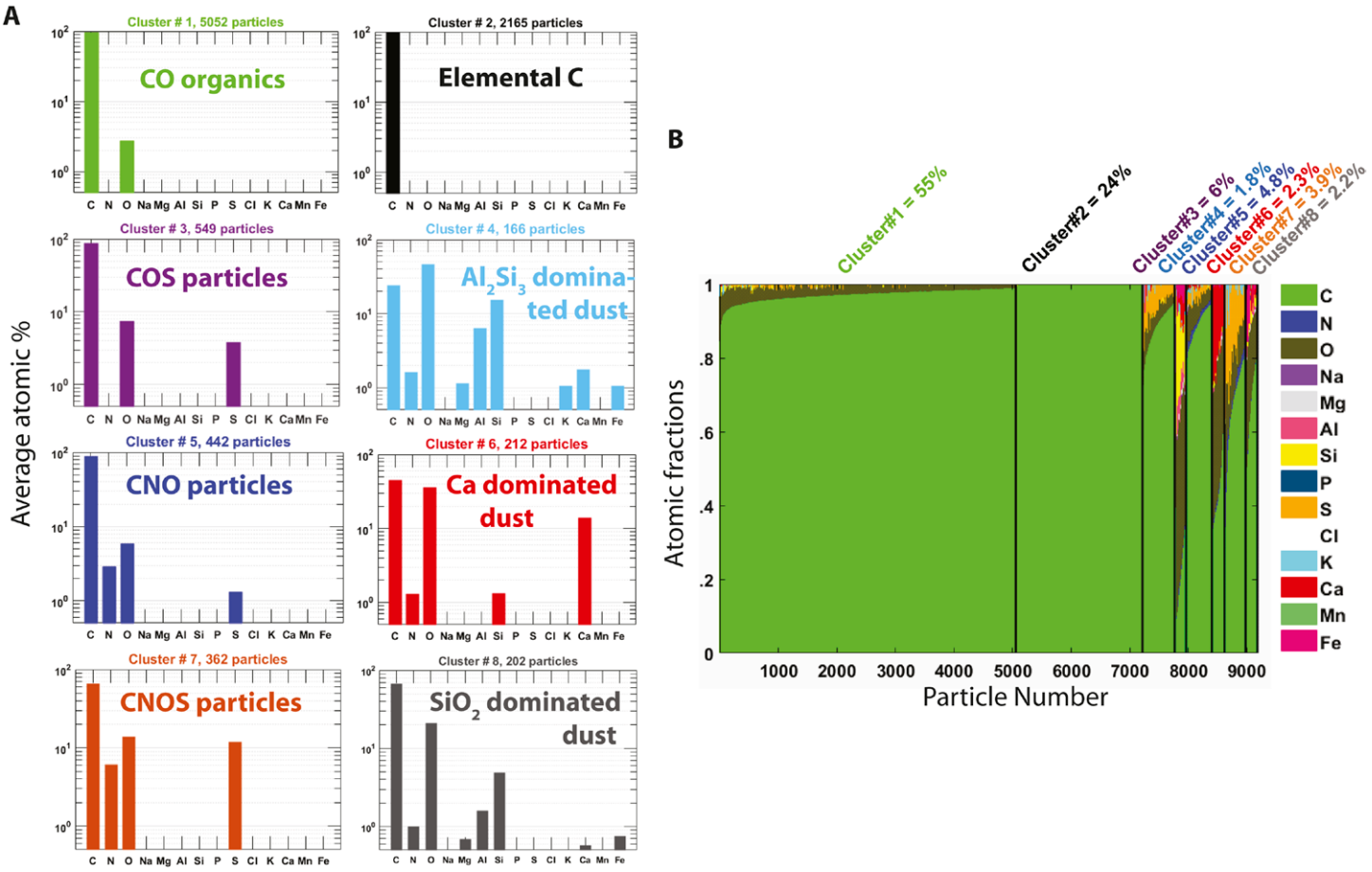

Fig. ES7. Major particle types identified by computer-controlled scanning electron microscopy with energy dispersive X-ray (CCSEM/EDX) analysis using *k*-means cluster analysis for ambient particle samples collected during the morning and afternoon of the closure case study on 15 Oct. (a) Identified particles types that exhibit significantly different atomic composition, where C: carbon; CO: carbon; oxygen; CNO: carbon, nitrogen, oxygen; COS: carbon, oxygen, sulfate; CNOS: carbon, nitrogen, oxygen, sulfate. (b) The distribution of identified particle types within all analyzed particles.

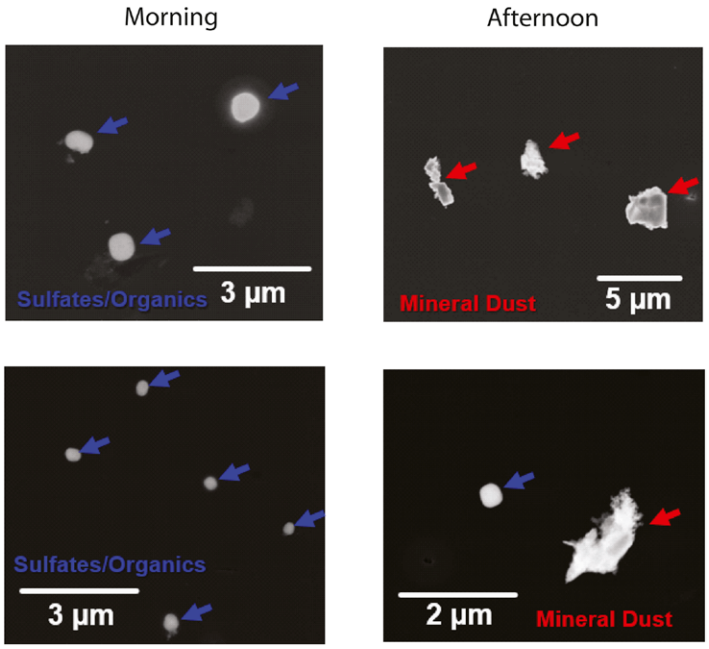

Fig. ES8. Exemplary scanning electron microscopy images of submicron ambient aerosol particles during morning and afternoon hours for the closure case study on 15 Oct.

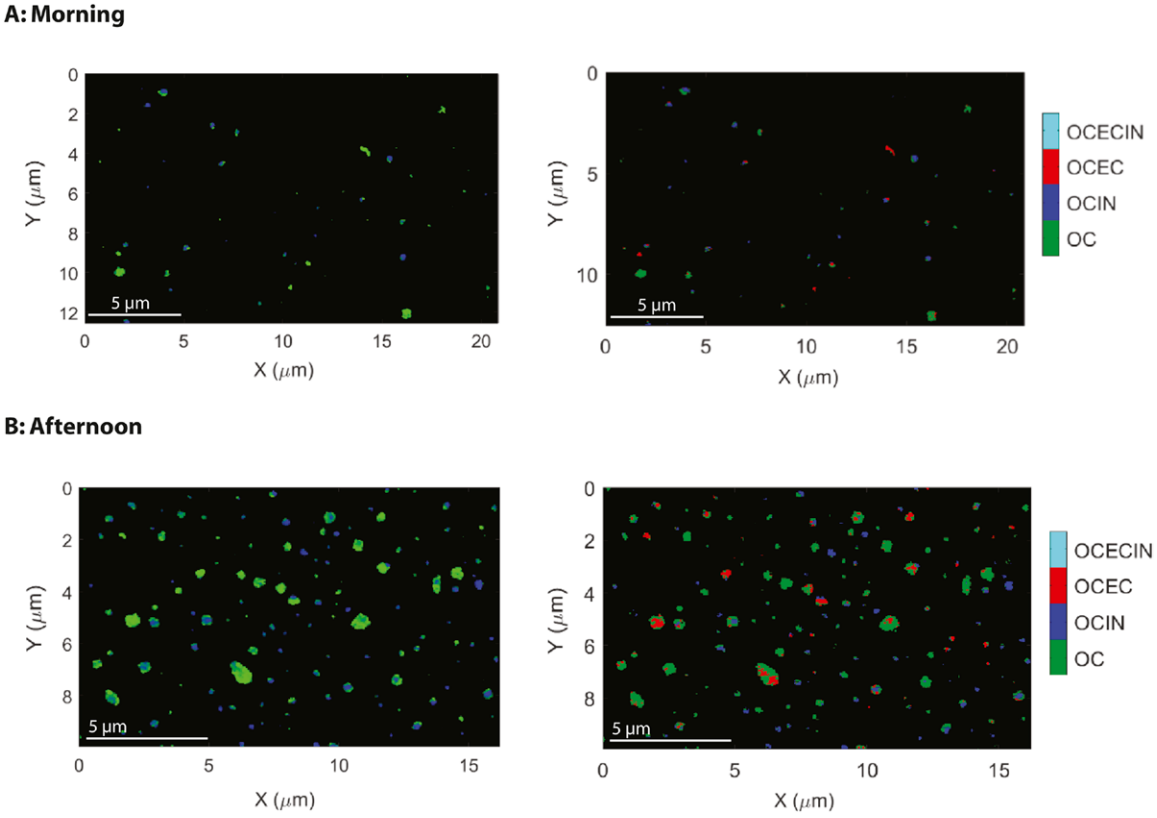

Fig. ES9. False-color particle composition maps derived from STXM/NEXAFS for (a) morning and (b) afternoon hours for closure case on 15 Oct. (left) The range of organics dominated particles (green) to inorganics dominated particles (blue). Blue color does not imply purely inorganic particles but that inorganic mass > 80%. (right) Particle mixing state where organic carbon (OC; green) represents organic matter with carboxyl groups, elemental carbon (EC; red) represents C-C double bonds, and inorganics (IN; blue). The *x* and *y* axes represent the coordinate system in micrometers. White line indicates the scale bar.

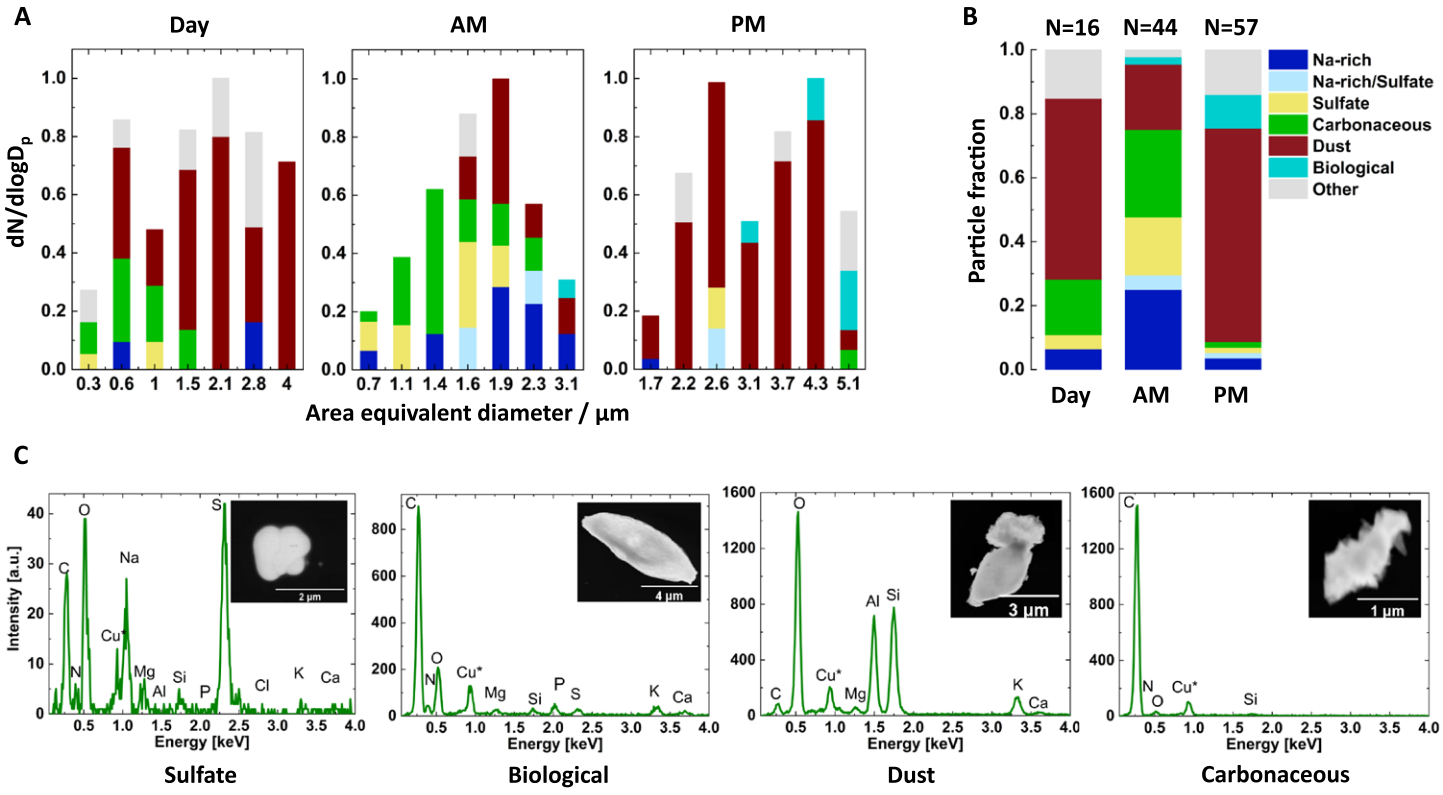

Fig. ES10. Scanning electron microscopy with energy dispersive X-ray (SEM/EDX) analysis of individual particles for samples collected during entire day (Day), morning (AM), and afternoon (PM) hours for closure case on 15 Oct. (a) Size-resolved particle-type classification for investigated time periods. (b) Overall particle-type distribution for investigated time periods. (c) Exemplary elemental composition analysis by energy dispersive X-ray spectroscopy of supermicron-sized particles and corresponding electron microscope image.

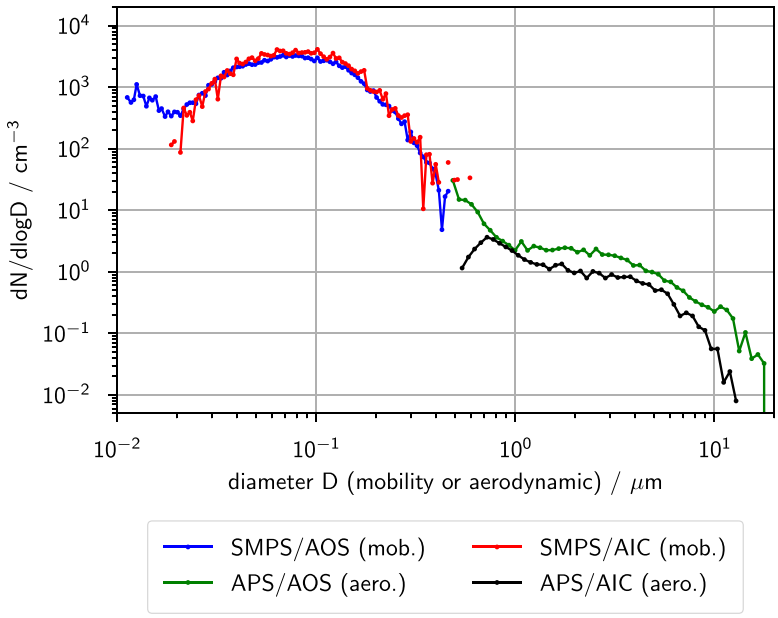

Fig. ES11. Comparing particle size distributions (PSDs) measured by the Southern Great Plains Atmospheric Observation system (SMPS/AOS and APS/AOS) and measured by the AEROICESTUDY (SMPS/AIC and APS/AIC). Note that the diameters are not yet unified, so both SMPS instruments measure mobility diameter and both APS instruments measure aerodynamic diameter. The count uncertainties scale with $N^{0.5}$; thus, within counting uncertainties good agreement within PSDs is achieved until 10-μm particle sizes.

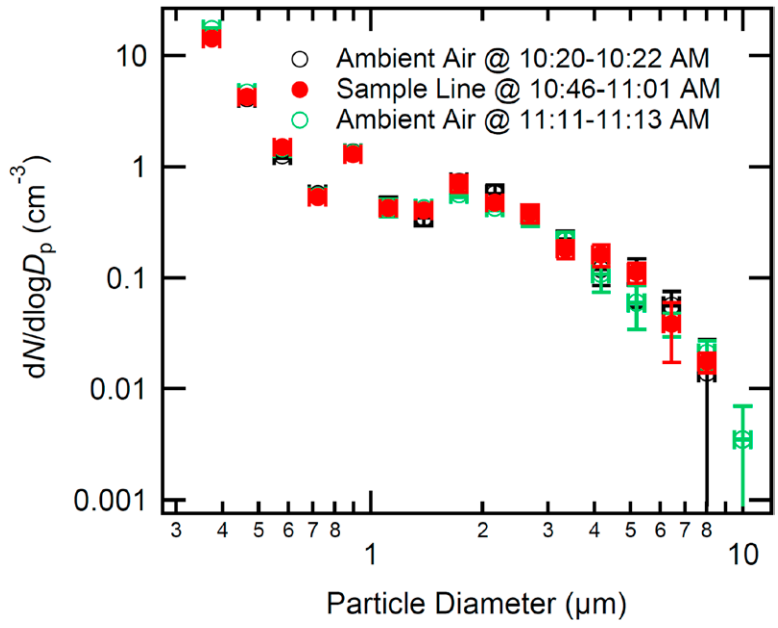

Fig. ES12. Particle stack and inlet losses for PINE-c. Aerosol particle size distributions for ambient particles at sampling stack inlet and through PINE-c sampling inlet connected to stack. Error bars represent ±5% size uncertainty and standard deviation of three measurements (1-min time average for each).

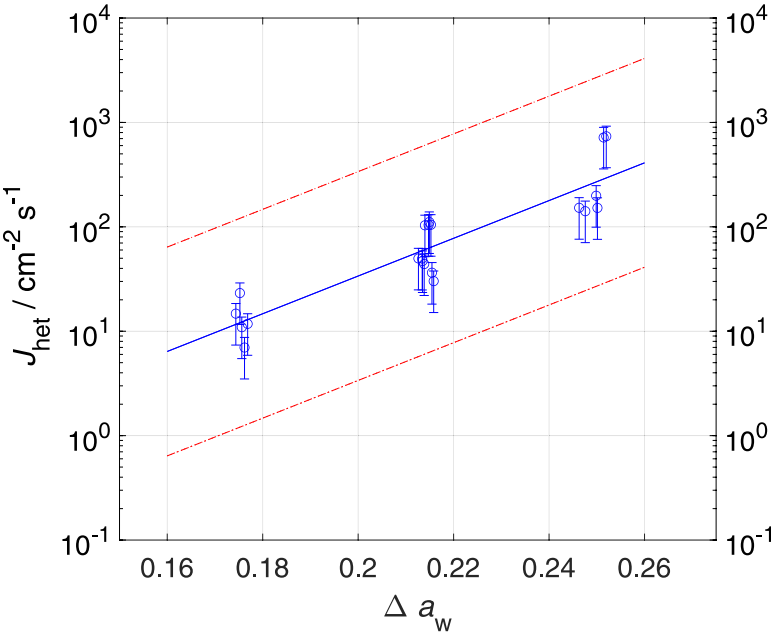

Fig. ES13. Water activity-based immersion freezing model (ABIFM) parameterization of soot acting as ice-nucleating particle derived from ice nucleation active sites (INAS) soot by Schill et al. (2020). The heterogeneous ice nucleation rate coefficient J_{het} is given as a function of the water activity criterion Δa_w with $\log_{10}(J_{het}) = c + m \times \Delta a_w$ and $m = 18.0679$ and $c = -2.0847$.

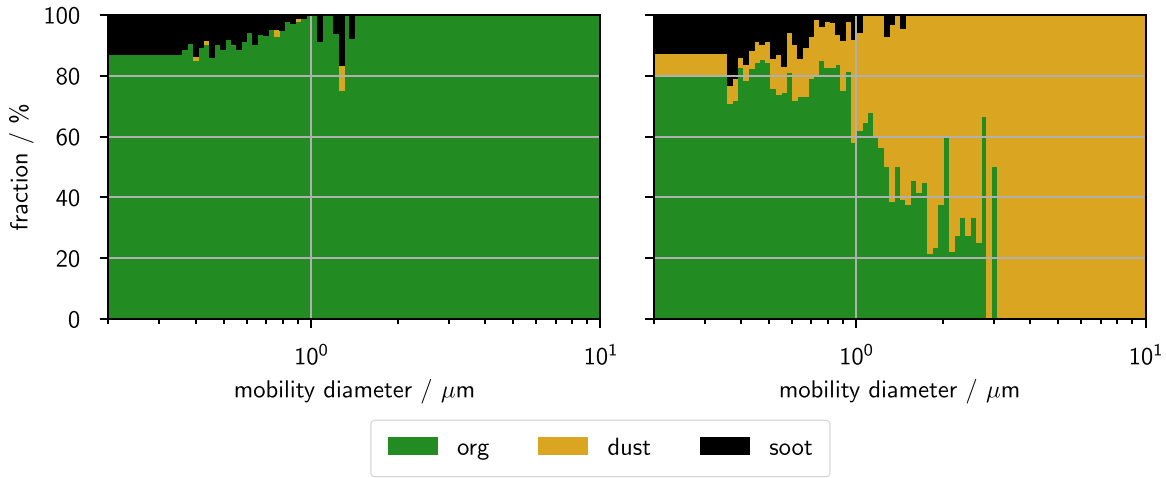

Fig. ES14. Approximated size-resolved aerosol composition for application in closure calculations for case study on 15 Oct. (a),(b) Mean aerosol composition for morning (0800–1030 LT) and afternoon (1400–1800 LT) hours, respectively. Black, green, and brown bins reflect soot, organic, and natural dust INPs, respectively. Soil-organic and biological INPs, not captured in closure, would be part of organic INP and mineral dust INP classes.

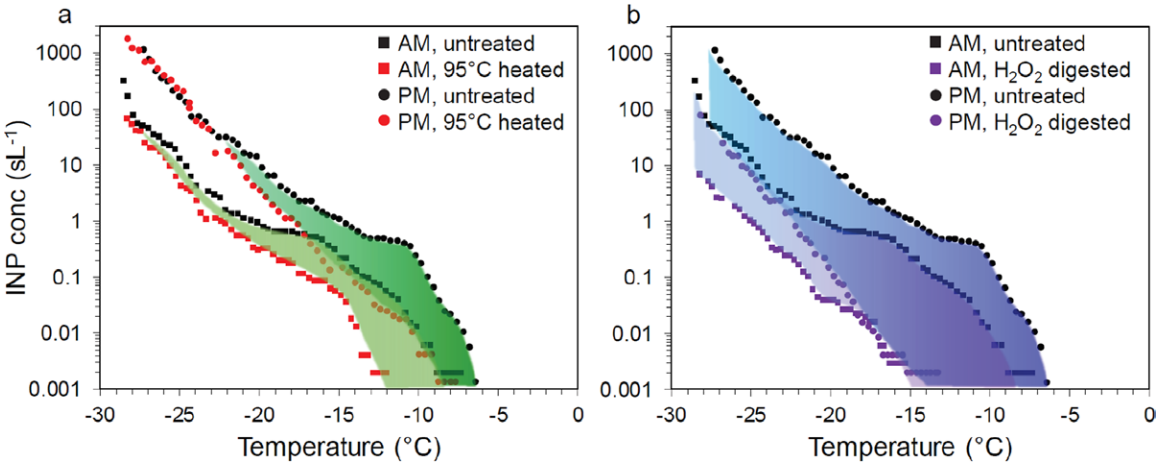

Fig. ES15. (a) Comparison of total INP concentrations, and the biological INP components of the totals, on the morning (0817–1057 LT) and afternoon (1340–1741 LT) on 15 Oct. Measures used filter collections followed by offline analysis using CSU's Ice Spectrometer. The biological component is defined as the number and proportion of the total that is denatured by heat (95°C for 20 min), shown by the green-shaded regions. Total INP concentrations and biological INP concentrations increased significantly between the morning and afternoon. The biological proportional component remained roughly constant at higher temperatures, accounting for >80% of INPs active warmer than –17°C, and ≥95% of INPs above –12°C, while the biological proportion at lower temperatures was immeasurable, especially in the afternoon. (b) Comparison of total INP concentrations, and the biological + organic INP components (blue shaded) of the totals in the morning and afternoon. The biological + organic INP component, defined as INPs removed by digestion with 10% H_2O_2 at 95°C, dominated the INP populations of both spectra at all temperatures. However, the residual inorganic, presumably mineral INP component (purple symbols) increased significantly in the afternoon, in step with the organic INPs that dominate at temperatures below about –22°C.

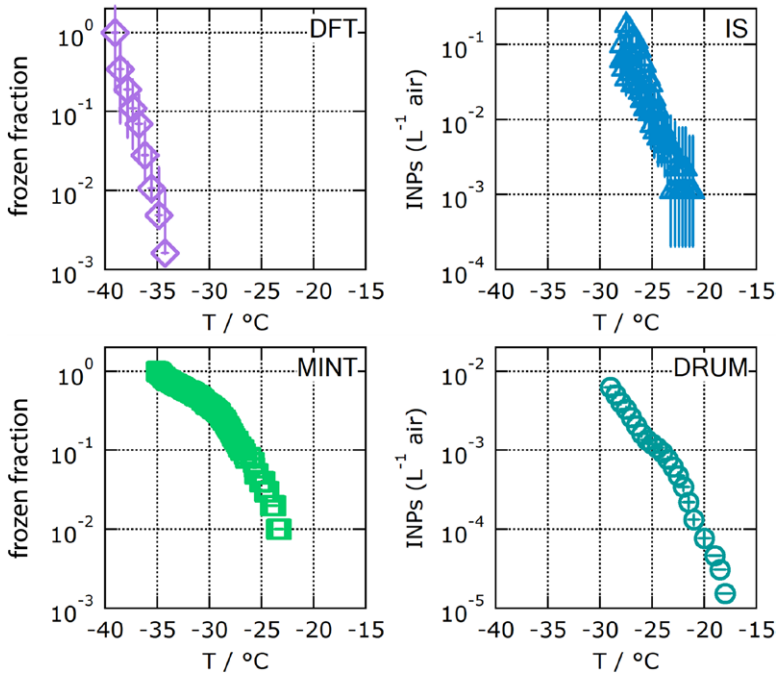

Fig. ES16. Offline immersion freezing blank experiments expressed as frozen fraction for Multi Orifice Uniform Deposition Impaction–Droplet Freezing Technique (MOUDI-DFT) and Microfluidic Ice Nucleation Technique (MINT) and as ice-nucleating particles (INPs) per liter of air for Ice Spectrometer (IS) and Davis Rotating-drum Unit for Monitoring (DRUM).

Table ES1. Sample information for case study on 15 Oct used for offline microspectroscopic analysis of ambient aerosol population by computer-controlled (CC) scanning electron microscopy (SEM) with energy dispersive X-ray (EDX) spectroscopy and scanning transmission X-ray microscopy (STXM) coupled with near-edge X-ray absorption fine structure spectroscopy (NEXAFS).

Analysis	Time period (LT)	MOUDI stages	Particle size, cutoff diameter (μm)	Particle numbers
CCSEM/EDX	0843–1004	5, 6	1, 0.56	2,422
CCSEM/EDX	1303–1750	4, 5, 6	1.8, 1, 0.56	3,262
SEM/EDX	0843–1004	3, 4, 5	3.2, 1.8, 1	44
SEM/EDX	1303–1750	3, 4	3.2, 1.8	57
SEM/EDX	0843–1750	1, 2	10, 5.6	46
STXM/NEXAFS	0843–1004	6, 8	0.32, 0.18	289
STXM/NEXAFS	1303–1750	6, 8	0.32, 0.18	568

Table ES2. Uncertainty in ice-nucleating particle (INP) number concentrations derived by propagation of uncertainties in aerosol number concentrations and immersion freezing parameterizations. See text for more details.

Parameterization	Quantity	Uncertainty estimate	Manner of propagation	Propagated uncertainty in INP conc.
DeMott et al. (2010)	Aerosol number concentration	±10%	Propagate through	±6%
DeMott et al. (2010)	Combined parameter uncertainty of parameterization	Factor of 7.5	Direct application	Factor of 7.5
DeMott et al. (2015)	Aerosol number concentration	±10%	Propagate through	±12%
DeMott et al. (2015)	Combined parameter uncertainty of parameterization	Factor of 4	Direct application	Factor of 4
INAS	Aerosol number concentration	±10%	Direct application	±10%
INAS dust	Ice-active surface site density, desert dust	Factor of 5, estimated from Fig. 6 in Niemand et al. (2012)	Propagate through	Factor of 5
INAS org	Ice-active surface site density, organics	Factor of 8.5, Fig. 3 in Knopf et al. (2013)	Propagate through	Factor of 8.5
INAS soot	Ice-active surface site density, soot	Factor of 10, Schill et al. (2020)	Propagate through	Factor of 10
ABIFM	Aerosol number concentration	±10%	Direct application	±10%
ABIFM dust	Coefficients to calculate J_{het} for desert dust	Factor of 2–40, Fig. 8 in Alpert and Knopf (2016)	Propagate through	Factor of 7.25 (range 2–40)
ABIFM org	Coefficients to calculate J_{het} for organics	Factor of 8.5, Fig. 3 in Knopf et al. (2013)	Propagate through	Factor of 8.5
ABIFM soot	Coefficients to calculate J_{het} for soot	Factor of 10, this study	Propagate through	Factor of 10

Table ES3. Predicted contribution of different INP size classes to total INP number concentrations measured by the Portable Ice Nucleation Experiment chamber (PINE-c) using the ice nucleation active sites (INAS) immersion freezing parameterization for the case study on 15 Oct.

	Time (CDT)	Temperature (°C)	INP (<5 μm) (1/L)	Fraction <1 μm (%)	Fraction 1–2.5 μm (%)	Fraction 2.5–5 μm (%)
1	0804	–24	1.38	99.38	0.49	0.13
2	0812	–28	17.82	99.10	0.44	0.46
3	0828	–24	1.14	99.48	0.47	0.05
4	0915	–20	0.17	99.56	0.44	0.00
5	0923	–24	1.15	99.42	0.51	0.07
6	0947	–22	0.46	99.59	0.39	0.02
			Average	99.42	0.46	0.12
1	1433	–22	10.66	29.74	9.34	60.92
2	1441	–26	118.66	20.53	9.08	70.39
3	1457	–28	381.91	17.48	12.50	70.02
4	1505	–18	1.14	32.93	8.43	58.64
5	1545	–18	1.06	35.32	8.45	56.23
6	1553	–22	6.83	44.25	8.24	47.50
7	1601	–28	124.36	48.22	10.03	41.75
8	1617	–26	46.24	49.88	7.41	42.72
			Average	34.79	9.18	56.02

Table ES4. Predicted contribution of different INP size classes to total INP number concentrations measured by the PINE-c using the water activity based immersion freezing model (ABIFM) parametrization for the case study on 15 Oct.

	Time (CDT)	Temperature (°C)	INP (<5 μm) (L–1)	Fraction <1 μm (%)	Fraction 1–2.5 μm (%)	Fraction 2.5–5 μm (%)
1	0804	–24	1.11	99.25	0.36	0.40
2	0812	–28	15.68	98.75	0.43	0.82
3	0828	–24	0.59	99.52	0.33	0.15
4	0915	–20	0.18	99.75	0.25	0.01
5	0923	–24	0.54	99.41	0.35	0.24
6	0947	–22	0.71	99.71	0.24	0.05
			Average	99.40	0.33	0.28
1	1433	–22	5.02	30.46	9.20	60.34
2	1441	–26	25.27	20.40	8.44	71.16
3	1457	–28	60.79	17.65	10.20	72.15
4	1505	–18	0.71	34.18	8.27	57.55
5	1545	–18	0.81	36.61	8.28	55.10
6	1553	–22	2.12	45.05	8.07	46.88
7	1601	–8	33.68	49.75	8.34	41.91
8	1617	–26	21.83	50.63	7.02	42.35
			Average	35.59	8.48	55.93

References

Agresti, A., and B. A. Coull, 1998: Approximate is better than "exact" for interval estimation of binomial proportions. *Amer. Stat.*, **52**, 119–126.

Alpert, P. A., and D. A. Knopf, 2016: Analysis of isothermal and cooling-rate-dependent immersion freezing by a unifying stochastic ice nucleation model. *Atmos. Chem. Phys.*, **16**, 2083–2107, https://doi.org/10.5194/acp-16-2083-2016.

——, J. Y. Aller, and D. A. Knopf, 2011: Ice nucleation from aqueous NaCl droplets with and without marine diatoms. *Atmos. Chem. Phys.*, **11**, 5539–5555, https://doi.org/10.5194/acp-11-5539-2011.

Beddows, D. C. S., M. Dall'osto, and R. M. Harrison, 2010: An enhanced procedure for the merging of atmospheric particle size distribution data measured using electrical mobility and time-of-flight analysers. *Aerosol Sci. Technol.*, **44**, 930–938, https://doi.org/10.1080/02786826.2010.502159.

Bi, K., and Coauthors, 2019: Measurements of ice nucleating particles in Beijing, China. *J. Geophys. Res. Atmos.*, **124**, 8065–8075, https://doi.org/10.1029/2019JD030609.

Brubaker, T., M. Polen, P. Cheng, V. Ekambaram, J. Somers, S. L. Anna, and R. C. Sullivan, 2020: Development and characterization of a "store and create" microfluidic device to determine the heterogeneous freezing properties of ice nucleating particles. *Aerosol Sci. Technol.*, **54**, 79–93, https://doi.org/10.1080/02786826.2019.1679349.

Cahill, T. A., P. J. Feeney, and R. A. Eldred, 1987: Size time composition profile of aerosols using the drum sampler. Nucl. Instrum. *Methods Phys. Res.*, **22B**, 344–348, https://doi.org/10.1016/0168-583X(87)90355-7.

Cheng, Y. Z., 1995: Mean shift, mode seeking, and clustering. *IEEE Trans. Pattern Anal. Mach. Intell.*, **17**, 790–799, https://doi.org/10.1109/34.400568.

China, S., and Coauthors, 2017: Ice cloud formation potential by free tropospheric particles from long-range transport over the northern Atlantic Ocean. *J. Geophys. Res. Atmos.*, **122**, 3065–3079, https://doi.org/10.1002/2016JD025817.

Connolly, P. J., O. Möhler, P. R. Field, H. Saathoff, R. Burgess, T. Choularton, and M. Gallagher, 2009: Studies of heterogeneous freezing by three different desert dust samples. *Atmos. Chem. Phys.*, **9**, 2805–2824, https://doi.org/10.5194/acp-9-2805-2009.

Corbin, J. C., and Coauthors, 2014: Mass spectrometry of refractory black carbon particles from six sources: Carbon-cluster and oxygenated ions. *Atmos. Chem. Phys.*, **14**, 2591–2603, https://doi.org/10.5194/acp-14-2591-2014.

Creamean, J. M., M. Maahn, G. de Boer, A. McComiskey, A. J. Sedlacek, and Y. Feng, 2018a: The influence of local oil exploration and regional wildfires on summer 2015 aerosol over the North Slope of Alaska. *Atmos. Chem. Phys.*, **18**, 555–570, https://doi.org/10.5194/acp-18-555-2018.

——, and Coauthors, 2018b: Marine and terrestrial influences on ice nucleating particles during continuous springtime measurements in an Arctic oilfield location. *Atmos. Chem. Phys.*, **18**, 18 023–18 042, https://doi.org/10.5194/acp-18-18023-2018.

——, and Coauthors, 2018c: HOVERCAT: A novel aerial system for evaluation of aerosol–cloud interactions. *Atmos. Meas. Tech.*, **11**, 3969–3985, https://doi.org/10.5194/amt-11-3969-2018.

——, C. Mignani, N. Bukowiecki, and F. Conen, 2019: Using freezing spectra characteristics to identify ice-nucleating particle populations during the winter in the Alps. *Atmos. Chem. Phys.*, **19**, 8123–8140, https://doi.org/10.5194/acp-19-8123-2019.

Dallmann, T. R., and Coauthors, 2014: Characterization of particulate matter emissions from on-road gasoline and diesel vehicles using a soot particle aerosol mass spectrometer. *Atmos. Chem. Phys.*, **14**, 7585–7599, https://doi.org/10.5194/acp-14-7585-2014.

Danabasoglu, G., and Coauthors, 2020: The Community Earth System Model version 2 (CESM2). *J. Adv. Model. Earth Syst.*, **12**, 35, https://doi.org/10.1029/2019MS001916.

DeMott, P. J., and Coauthors, 2010: Predicting global atmospheric ice nuclei distributions and their impacts on climate. *Proc. Natl. Acad. Sci. USA*, **107**, 11 217–11 222, https://doi.org/10.1073/pnas.0910818107.

——, and Coauthors, 2015: Integrating laboratory and field data to quantify the immersion freezing ice nucleation activity of mineral dust particles. *Atmos. Chem. Phys.*, **15**, 393–409, https://doi.org/10.5194/acp-15-393-2015.

——, and Coauthors, 2018: The Fifth International Workshop on Ice Nucleation phase 2 (FIN-02): Laboratory intercomparison of ice nucleation measurements. *Atmos. Meas. Tech.*, **11**, 6231–6257, https://doi.org/10.5194/amt-11-6231-2018.

Fraund, M., T. Park, L. Yao, D. Bonanno, D. Q. Pham, and R. C. Moffet, 2019: Quantitative capabilities of STXM to measure spatially resolved organic volume fractions of mixed organic/inorganic particles. *Atmos. Meas. Tech.*, **12**, 1619–1633, https://doi.org/10.5194/amt-12-1619-2019.

Fukunaga, K., and L. D. Hostetler, 1975: Estimation of gradient of a density-function, with applications in pattern-recognition. *IEEE Trans. Inf. Theory*, **21**, 32–40, https://doi.org/10.1109/TIT.1975.1055330.

Gelaro, R., and Coauthors, 2017: The Modern-Era Retrospective Analysis for Research and Applications, version 2 (MERRA-2). *J. Climate*, **30**, 5419–5454, https://doi.org/10.1175/JCLI-D-16-0758.1.

Gemayel, R., S. Hellebust, B. Temime-Roussel, N. Hayeck, J. T. Van Elteren, H. Wortham, and S. Gligorovski, 2016: The performance and the characterization of laser ablation aerosol particle time-of-flight mass spectrometry (LAAP-ToF-MS). *Atmos. Meas. Tech.*, **9**, 1947–1959, https://doi.org/10.5194/amt-9-1947-2016.

Ghorai, S., and A. V. Tivanski, 2010: Hygroscopic behavior of individual submicrometer particles studied by X-ray spectromicroscopy. *Anal. Chem.*, **82**, 9289–9298, https://doi.org/10.1021/ac101797k.

——, A. Laskin, and A. V. Tivanski, 2011: Spectroscopic evidence of keto-enol tautomerism in deliquesced malonic acid particles. *J. Phys. Chem.*, **115A**, 4373–4380, https://doi.org/10.1021/jp112360x.

Hiranuma, N., and Coauthors, 2015: A comprehensive laboratory study on the immersion freezing behavior of illite NX particles: A comparison of 17 ice nucleation measurement techniques. *Atmos. Chem. Phys.*, **15**, 2489–2518, https://doi.org/10.5194/acp-15-2489-2015.

Hopkins, R. J., and Coauthors, 2007: Correlations between optical, chemical and physical properties of biomass burn aerosols. *Geophys. Res. Lett.*, **34**, L18806, https://doi.org/10.1029/2007GL030502.

——, and Coauthors, 2008: Chemical speciation of sulfur in marine cloud droplets and particles: Analysis of individual particles from the marine boundary layer over the California Current. *J. Geophys. Res.*, **113**, D04209, https://doi.org/10.1029/2007JD008954.

Jahn, L. G., M. J. Polen, L. G. Jahl, T. A. Brubaker, J. Somers, and R. C. Sullivan, 2020: Biomass combustion produces ice-active minerals in biomass-burning aerosol and bottom ash. *Proc. Natl. Acad. Sci. USA*, **117**, 21 928–21 937, https://doi.org/10.1073/pnas.1922128117.

Khlystov, A., C. Stanier, and S. N. Pandis, 2004: An algorithm for combining electrical mobility and aerodynamic size distributions data when measuring ambient aerosol. *Aerosol Sci. Technol.*, **38** (Suppl.), 229–238, https://doi.org/10.1080/02786820390229543.

Kilcoyne, A. L. D., and Coauthors, 2003: Interferometer-controlled scanning transmission X-ray microscopes at the Advanced Light Source. *J. Synchrotron Radiat.*, **10**, 125–136, https://doi.org/10.1107/S0909049502017739.

Knopf, D. A., and P. A. Alpert, 2013: A water activity based model of heterogeneous ice nucleation kinetics for freezing of water and aqueous solution droplets. *Faraday Discuss.*, **165**, 513–534, https://doi.org/10.1039/c3fd00035d.

——, ——, B. Wang, and J. Y. Aller, 2011: Stimulation of ice nucleation by marine diatoms. *Nat. Geosci.*, **4**, 88–90, https://doi.org/10.1038/ngeo1037.

——, and Coauthors, 2014: Microspectroscopic imaging and characterization of individually identified ice nucleating particles from a case field study. *J. Geophys. Res. Atmos.*, **119**, 10 365–10 381, https://doi.org/10.1002/2014JD021866.

——, P. A. Alpert, and B. Wang, 2018: The role of organic aerosol in atmospheric ice nucleation: A review. *ACS Earth Space Chem.*, **2**, 168–202, https://doi.org/10.1021/acsearthspacechem.7b00120.

——, ——, A. Zipori, N. Reicher, and Y. Rudich, 2020: Stochastic nucleation processes and substrate abundance explain time-dependent freezing in supercooled droplets. *Climate Atmos. Sci*., **3**, 2, https://doi.org/10.1038/s41612-020-0106-4.

Kok, J. F., 2011: A scaling theory for the size distribution of emitted dust aerosols suggests climate models underestimate the size of the global dust cycle. *Proc. Natl. Acad. Sci. USA*, **108**, 1016–1021, https://doi.org/10.1073/pnas.1014798108.

Koop, T., B. P. Luo, U. M. Biermann, P. J. Crutzen, and T. Peter, 1997: Freezing of HNO3/H2SO4/H2O solutions at stratospheric temperatures: Nucleation statistics and experiments. *J. Phys. Chem.*, **101A**, 1117–1133, https://doi.org/10.1021/jp9626531.

——, ——, A. Tsias, and T. Peter, 2000: Water activity as the determinant for homogeneous ice nucleation in aqueous solutions. *Nature*, **406**, 611–614, https://doi.org/10.1038/35020537.

Kyrouac, J., and D. Holdridge, 2019: Atmospheric Radiation Measurement (ARM) user facility, 1993, surface meteorological instrumentation (MET), 2019-10-15 to 2019-10-15, Southern Great Plains (SGP) Lamont, OK (extended and co-located with C1) (E13) (updated hourly). ARM Climate Research Facility Data Archive, accessed 17 December 2020, https://doi.org/10.5439/1025220.

Laskin, A., J. P. Cowin, and M. J. Iedema, 2006: Analysis of individual environmental particles using modern methods of electron microscopy and X-ray microanalysis. *J. Electron Spectrosc.*, **150**, 260–274, https://doi.org/10.1016/j.elspec.2005.06.008.

——, M. K. Gilles, D. A. Knopf, B. B. Wang, and S. China, 2016: Progress in the analysis of complex atmospheric particles. *Annu. Rev. Anal. Chem.*, **9**, 117–143, https://doi.org/10.1146/annurev-anchem-071015-041521.

——, R. C. Moffet, and M. K. Gilles, 2019: Chemical imaging of atmospheric particles. *Acc. Chem. Res.*, **52**, 3419–3431, https://doi.org/10.1021/acs.accounts.9b00396.

Liu, X., and Coauthors, 2016: Description and evaluation of a new four-mode version of the Modal Aerosol Module (MAM4) within version 5.3 of the Community Atmosphere Model. *Geosci. Model Dev.*, **9**, 505–522, https://doi.org/10.5194/gmd-9-505-2016.

Mason, R. H., and Coauthors, 2015: The micro-orifice uniform deposit impactor-droplet freezing technique (MOUDI-DFT) for measuring concentrations of ice nucleating particles as a function of size: Improvements and initial validation. *Atmos. Meas. Tech.*, **8**, 2449–2462, https://doi.org/10.5194/amt-8-2449-2015.

McCluskey, C. S., and Coauthors, 2018: Marine and terrestrial organic ice-nucleating particles in pristine marine to continentally influenced northeast Atlantic air masses. *J. Geophys. Res.*, **123**, 6196–6212, https://doi.org/10.1029/2017JD028033.

Moffet, R. C., A. V. Tivanski, and M. K. Gilles, 2010a: Scanning X-ray transmission microscopy: Applications in atmospheric aerosol research. *Fundamentals and Applications in Aerosol Spectroscopy*, R. Signorell and J. P. Reid, Eds., Taylor and Francis, 419–462.

——, T. Henn, A. Laskin, and M. K. Gilles, 2010b: Automated chemical analysis of internally mixed aerosol particles using X-ray spectromicroscopy at the carbon K-edge. *Anal. Chem.*, **82**, 7906–7914, https://doi.org/10.1021/ac1012909.

——, and Coauthors, 2013: Spectro-microscopic measurements of carbonaceous aerosol aging in central California. *Atmos. Chem. Phys*., **13**, 10 445–10 459, https://doi.org/10.5194/acp-13-10445-2013.

——, and Coauthors, 2016: Morphology and mixing of black carbon particles collected in central California during the CARES field study. *Atmos. Chem. Phys.*, **16**, 14 515–14 525, https://doi.org/10.5194/acp-16-14515-2016.

Möhler, O., and Coauthors, 2003: Experimental investigation of homogeneous freezing of sulphuric acid particles in the aerosol chamber AIDA. *Atmos. Chem. Phys.*, **3**, 211–223, https://doi.org/10.5194/acp-3-211-2003.

——, and Coauthors, 2021: The Portable Ice Nucleation Experiment (PINE): A new online instrument for laboratory studies and automated long-term field observations of ice-nucleating particles. *Atmos. Meas. Tech.*, **14**, 1143–1166, https://doi.org/10.5194/amt-14-1143-2021.

Moore, K. A., 2020: Constraining marine ice nucleating particle parameterizations in atmospheric models using observations from the Southern Ocean. Colorado State University Dept. of Atmospheric Science Rep., 105 pp.

Murphy, D. M., 2007: The design of single particle laser mass spectrometers. *Mass Spectrom. Rev.*, **26**, 150–165, https://doi.org/10.1002/mas.20113.

Niemand, M., and Coauthors, 2012: A particle-surface-area-based parameterization of immersion freezing on desert dust particles. *J. Atmos. Sci.*, **69**, 3077–3092, https://doi.org/10.1175/JAS-D-11-0249.1.

O'Brien, R. E., and Coauthors, 2015: Chemical imaging of ambient aerosol particles: Observational constraints on mixing state parameterization. *J. Geophys. Res. Atmos.*, **120**, 9591–9605, https://doi.org/10.1002/2015JD023480.

Onasch, T. B., and Coauthors, 2012: Soot particle aerosol mass spectrometer: Development, validation, and initial application. *Aerosol Sci. Technol.*, **46**, 804–817, https://doi.org/10.1080/02786826.2012.663948.

Perring, A. E., and Coauthors, 2015: Airborne observations of regional variation in fluorescent aerosol across the United States. *J. Geophys. Res. Atmos.*, **120**, 1153–1170, https://doi.org/10.1002/2014JD022495.

Pöhlker, C., J. A. Huffman, and U. Pöschl, 2012: Autofluorescence of atmospheric bioaerosols—Fluorescent biomolecules and potential interferences. *Atmos. Meas. Tech.*, **5**, 37–71, https://doi.org/10.5194/amt-5-37-2012.

Polen, M., T. Brubaker, J. Somers, and R. C. Sullivan, 2018: Cleaning up our water: Reducing interferences from nonhomogeneous freezing of "pure" water in droplet freezing assays of ice-nucleating particles. *Atmos. Meas. Tech.*, **11**, 5315–5334, https://doi.org/10.5194/amt-11-5315-2018.

Pratt, K. A., and K. A. Prather, 2012: Mass spectrometry of atmospheric aerosols—Recent developments and applications. Part II: On-line mass spectrometry techniques. *Mass Spectrom. Rev.*, **31**, 17–48, https://doi.org/10.1002/mas.20330.

Pruppacher, H. R., and J. D. Klett, 1997: *Microphysics of Clouds and Precipitation*. 2nd ed. Kluwer Academic, 954 pp.

Rebotier, T. P., and K. A. Prather, 2007: Aerosol time-of-flight mass spectrometry data analysis: A benchmark of clustering algorithms. *Anal. Chim. Acta*, **585**, 38–54, https://doi.org/10.1016/j.aca.2006.12.009.

Reitz, P., S. R. Zorn, S. H. Trimborn, and A. M. Trimborn, 2016: A new, powerful technique to analyze single particle aerosol mass spectra using a combination of OPTICS and the fuzzy c-means algorithm. *J. Aerosol Sci.*, **98**, 1–14, https://doi.org/10.1016/j.jaerosci.2016.04.003.

Rigg, Y. J., P. A. Alpert, and D. A. Knopf, 2013: Immersion freezing of water and aqueous ammonium sulfate droplets initiated by humic-like substances as a function of water activity. *Atmos. Chem. Phys.*, **13**, 6603–6622, https://doi.org/10.5194/acp-13-6603-2013.

Rogers, D. C., 1988: Development of a continuous flow thermal gradient diffusion chamber for ice nucleation studies. *Atmos. Res.*, **22**, 149–181, https://doi.org/10.1016/0169-8095(88)90005-1.

——, P. J. DeMott, S. M. Kreidenweis, and Y. L. Chen, 2001: A continuous-flow diffusion chamber for airborne measurements of ice nuclei. *J. Atmos. Oceanic Technol.*, **18**, 725–741, https://doi.org/10.1175/1520-0426(2001)018<0725:ACFDCF>2.0.CO;2.

Schill, G. P., and Coauthors, 2020: The contribution of black carbon to global ice nucleating particle concentrations relevant to mixed-phase clouds. *Proc. Natl. Acad. Sci. USA*, **117**, 22 705–22 711, https://doi.org/10.1073/pnas.2001674117.

Selim, S. Z., and M. A. Ismail, 1984: K-means-type algorithms—A generalized convergence theorem and characterization of local optimality. *IEEE Trans. Pattern Anal. Mach. Intell.*, **6**, 81–87, https://doi.org/10.1109/TPAMI.1984.4767478.

Shen, X. L., R. Ramisetty, C. Mohr, W. Huang, T. Leisner, and H. Saathoff, 2018: Laser ablation aerosol particle time-of-flight mass spectrometer (LAAPTOF): Performance, reference spectra and classification of atmospheric samples. *Atmos. Meas. Tech.*, **11**, 2325–2343, https://doi.org/10.5194/amt-11-2325-2018.

Sullivan, R. C., and K. A. Prather, 2005: Recent advances in our understanding of atmospheric chemistry and climate made possible by on-line

aerosol analysis instrumentation. *Anal. Chem.*, **77**, 3861–3885, https://doi.org/10.1021/ac050716i.

Suski, K. J., T. C. J. Hill, E. J. T. Levin, A. Miller, P. J. DeMott, and S. M. Kreidenweis, 2018: Agricultural harvesting emissions of ice-nucleating particles. *Atmos. Chem. Phys.*, **18**, 13 755–13 771, https://doi.org/10.5194/acp-18-13755-2018.

Thompson, S. K., 1987: Sample-size for estimating multinomial proportions. *Amer. Stat.*, **41**, 42–46.

Tobo, Y., and Coauthors, 2013: Biological aerosol particles as a key determinant of ice nuclei populations in a forest ecosystem. *J. Geophys. Res. Atmos.*, **118**, 10 100–10 110, https://doi.org/10.1002/jgrd.50801.

Twohy, C. H., and Coauthors, 2016: Abundance of fluorescent biological aerosol particles at temperatures conducive to the formation of mixed-phase and cirrus clouds. *Atmos. Chem. Phys.*, **16**, 8205–8225, https://doi.org/10.5194/acp-16-8205-2016.

Vali, G., 1971: Quantitative evaluation of experimental results on heterogeneous freezing nucleation of supercooled liquids. *J. Atmos. Sci.*, **28**, 402–409, https://doi.org/10.1175/1520-0469(1971)028<0402:QEOERA>2.0.CO;2.

——, 2019: Revisiting the differential freezing nucleus spectra derived from drop-freezing experiments: Methods of calculation, applications, and confidence limits. *Atmos. Meas. Tech.*, **12**, 1219–1231, https://doi.org/10.5194/amt-12-1219-2019.

——, P. J. DeMott, O. Mohler, and T. F. Whale, 2015: A proposal for ice nucleation terminology. *Atmos. Chem. Phys.*, **15**, 10 263–10 270, https://doi.org/10.5194/acp-15-10263-2015.

Wang, B., A. Laskin, T. Roedel, M. K. Gilles, R. C. Moffet, A. V. Tivanski, and D. A. Knopf, 2012: Heterogeneous ice nucleation and water uptake by field-collected atmospheric particles below 273 K. *J. Geophys. Res.*, **117**, D00V19, https://doi.org/10.1029/2012JD017446.

Zender, C. S., H. S. Bian, and D. Newman, 2003: Mineral Dust Entrainment and Deposition (DEAD) model: Description and 1990s dust climatology. *J. Geophys. Res.*, **108**, 4416, https://doi.org/10.1029/2002JD002775.